Rapid mapping of ultrafine fault zone topography with structure from motion

Kendra Johnson[1], Edwin Nissen[1], Srikanth Saripalli[2], J Ramón Arrowsmith[2], Patrick McGarey[2], Katherine Scharer[3], Patrick Williams[4], and Kimberly Blisniuk[5]

[1]*Department of Geophysics, Colorado School of Mines, 1500 Illinois Street, Golden, Colorado 80401, USA*
[2]*School of Earth and Space Exploration, Arizona State University, 1151 S. Forest Avenue, Tempe, Arizona 85281, USA*
[3]*U.S. Geological Survey, 525 S. Wilson Avenue, Pasadena, California 91106, USA*
[4]*San Diego State University, 5500 Campanile Drive, San Diego, California 92182, USA*
[5]*Department of Earth and Planetary Science, University of California, Berkeley, 2455 Ridge Road, Berkeley, California 94709, USA*

ABSTRACT

Structure from Motion (SfM) generates high-resolution topography and coregistered texture (color) from an unstructured set of overlapping photographs taken from varying viewpoints, overcoming many of the cost, time, and logistical limitations of Light Detection and Ranging (LiDAR) and other topographic surveying methods. This paper provides the first investigation of SfM as a tool for mapping fault zone topography in areas of sparse or low-lying vegetation. First, we present a simple, affordable SfM workflow, based on an unmanned helium balloon or motorized glider, an inexpensive camera, and semiautomated software. Second, we illustrate the system at two sites on southern California faults covered by existing airborne or terrestrial LiDAR, enabling a comparative assessment of SfM topography resolution and precision. At the first site, an ~0.1 km² alluvial fan on the San Andreas fault, a colored point cloud of density mostly >700 points/m² and a 3 cm digital elevation model (DEM) and orthophoto were produced from 233 photos collected ~50 m above ground level. When a few global positioning system ground control points are incorporated, closest point vertical distances to the much sparser (~4 points/m²) airborne LiDAR point cloud are mostly <3 cm. The second site spans an ~1 km section of the 1992 Landers earthquake scarp. A colored point cloud of density mostly >530 points/m² and a 2 cm DEM and orthophoto were produced from 450 photos taken from ~60 m above ground level. Closest point vertical distances to existing terrestrial LiDAR data of comparable density are mostly <6 cm. Each SfM survey took ~2 h to complete and several hours to generate the scene topography and texture. SfM greatly facilitates the imaging of subtle geomorphic offsets related to past earthquakes as well as rapid response mapping or long-term monitoring of faulted landscapes.

INTRODUCTION

The recent and significant increase in availability of high-resolution digital topography along many active faults has provided new means of characterizing tectonically active landscapes (e.g., Frankel and Dolan, 2007; Hilley et al., 2010; Meigs, 2013), mapping previously undetected fault scarps (e.g., Haugerud et al., 2003; Cunningham et al., 2006; Kondo et al., 2008), and measuring subtle geomorphic offsets related to modern, historic, and prehistoric surface-rupturing earthquakes (e.g., Hudnut et al., 2002; Prentice et al., 2010; Zielke et al., 2010, 2012). These rich new data sets facilitate new types of fault behavior studies that help better characterize seismic hazard. High-resolution topography also offers powerful new insights in numerous other Earth science fields, including process geomorphology, hydrology, sedimentology, and structural geology. Airborne and terrestrial light detection and ranging (LiDAR) are currently the most prevalent techniques for generating such data, but the high costs and logistical demands of these laser-based mapping techniques can restrict their utilization.

In the past few years, an affordable mapping method called structure from motion (SfM) has been developed in which the structure of the scene, that is, the shape (topography) and texture (color) of the ground surface, as well as the camera positions and orientations, is reconstructed using overlapping photographs from multiple viewpoints. The method utilizes recent advances in feature-matching algorithms that allow for large changes in scale, perspective, and even occlusion (Lowe, 2004), making photoset acquisition much more straightforward than in traditional photogrammetry (Snavely et al., 2008). While not originally intended for geological applications, geoscientists have adopted SfM as a method of mapping fine-scale topography in a variety of sparsely vegetated environments (Harwin and Lucieer, 2012; James and Robson, 2012; Westoby et al., 2012; Fonstad et al., 2013). Hitherto, its suitability for mapping fault zone topography, including in rapid response to an earthquake, has not been demonstrated. Furthermore, the precision and resolution of SfM topography, especially in relation to data generated with airborne or terrestrial LiDAR, are not yet clear. This paper addresses these issues using sample SfM and LiDAR topography from semiarid tectonic landscapes along active faults in southern California.

We begin by summarizing the advantages and disadvantages of airborne and terrestrial LiDAR surveying for mapping fault zone topography, helping frame our subsequent consideration for the merits of SfM as an alternative technology. We then describe the principles of SfM and summarize the few previous studies that have used this new technology to map natural landscapes. Next, we introduce an affordable SfM mapping system that can rapidly generate subdecimeter-resolution digital elevation models (DEMs) and coregistered orthophotos, and is easily deployed by a person working alone. The method requires only an inexpensive unmanned aerial vehicle (UAV) or helium balloon, a consumer-grade digital camera with an internal or external global positioning system (GPS) tagger, and commercially available software. We then use our aerial SfM system to map two field sites along major active faults in southern California, choosing areas where we are able

Geosphere; October 2014; v. 10; no. 5; p. 969–986; doi:10.1130/GES01017.1; 13 figures; 1 table.
Received 16 December 2013 ♦ Revision received 15 April 2014 ♦ Accepted 3 July 2014 ♦ Published online 18 August 2014

to compare the quality of the resulting digital topography with airborne and terrestrial LiDAR data. This enables a quantitative comparison of the accuracy and precision of SfM and LiDAR topography, and also qualitatively demonstrates how SfM reveals geomorphic offsets that were not clearly imaged by LiDAR. Finally, we discuss the application for this technology in the field of tectonic geomorphology.

BACKGROUND

Airborne and Terrestrial Lidar

In the past decade, airborne and terrestrial LiDAR have rapidly gained popularity as methods for producing detailed maps of tectonic landscapes due to their orders-of-magnitude improvement in topographic accuracy and resolution over existing topographic maps, including satellite-derived elevation data sets (e.g., the 30 m Advanced Spaceborne Thermal Emission and Reflection Radiometer Global DEM and 90 m Shuttle Radar Topography Mission data sets; Hayakawa et al., 2008). These laser scanning methods are shown schematically in Figures 1A and 1B.

Traditional airborne LiDAR, also called Airborne Laser Swath Mapping (ALSM), consists of a laser scanner with kinematic GPS and inertial measurement systems on an airplane platform that sweeps over a scene, determining the elevation of points on the ground by combining return times of reflected or backscattered laser pulses with the known position (x, y, and z) and orientation (pitch, roll, and yaw) of the platform (Fig. 1A). The converted returns form a point cloud, which can be gridded or triangulated into a DEM. The earliest airborne LiDAR surveys, flown in the 1990s, produced point clouds with densities of <1 point/m^2 (e.g., Ridgway et al., 1997; Shrestha et al., 1999; Bielecki and Mueller, 2002), but with higher scanner pulse rates, modern airborne LiDAR surveys can generate point clouds with >10 points/m^2. Such point spacings are finer than the average amount of surface slip typically observed in large, ground-rupturing earthquakes, and have enabled airborne LiDAR to image geomorphic offsets generated in modern, historic, or prehistoric events (e.g., Hudnut et al., 2002; Prentice et al., 2010; Zielke et al., 2010, 2012; Elliott et al., 2012; Oskin et al., 2012; Quigley et al., 2012; Salisbury et al., 2012; Scharer et al., 2014). These surveys span several hundred square kilometers, areas that are not feasible with ground-based mapping systems or low-cost aerial platforms.

Airborne LiDAR outperforms optical imagery in its ability to penetrate vegetation at most sites. Modern sensors can record multiple returns, such as those reflected from the top of the canopy, within the canopy, and the ground; by using only the last returns, most vegetation can be stripped from the scene. Haugerud et al. (2003), Cunningham et al. (2006), Barth et al. (2012), Howle et al. (2012), and Lin et al. (2013) employed this capability to detect fault scarps in heavily forested areas of the western United States, eastern Europe, New Zealand, and Japan. Similarly, Kondo et al. (2008) removed airborne LiDAR returns from buildings to reveal a previously unrecognized fault scarp in an urban setting in Japan.

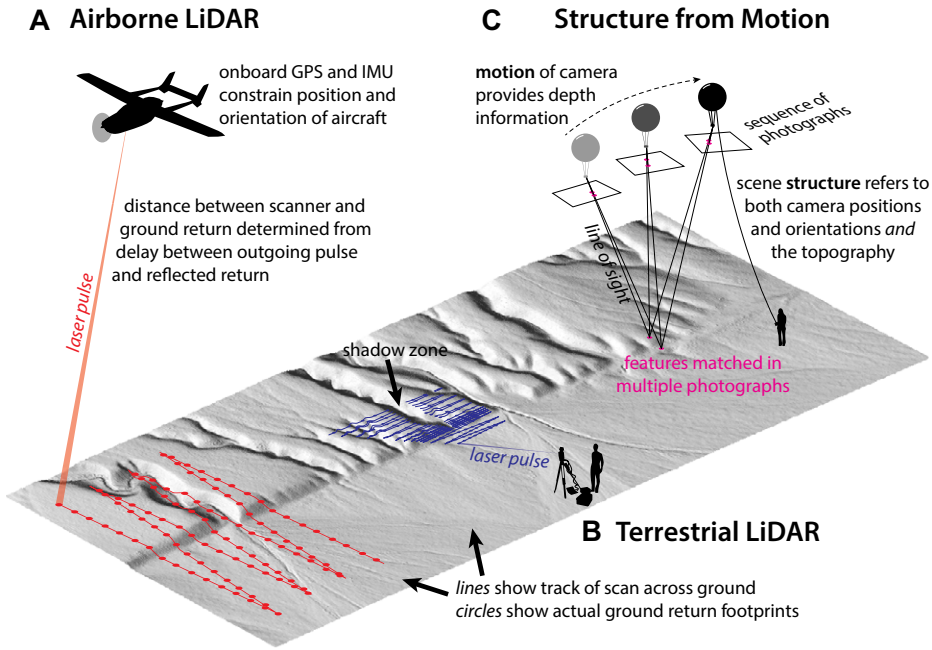

Figure 1. A schematic illustration of three methods of producing high-resolution digital topography discussed in the text. (A) Airborne LiDAR (light detection and ranging). GPS—global positioning system; IMU—inertial measurement unit. (B) Terrestrial LiDAR. (C) Aerial platform-based structure from motion (SfM).

The major disadvantages of airborne LiDAR include the expensive requirement of a piloted airplane carrying specialist laser scanning equipment. Survey costs typically reach thousands of dollars per square kilometer for small target areas, and several hundred dollars per square kilometer for the largest data sets. Ground-based GPS reference stations are often used to improve the positioning of the airplane, requiring additional trained personnel. The necessary logistical planning for large LiDAR surveys therefore makes rapid or repeat deployment difficult, although a few paired or multitemporal data sets exist (e.g., Shrestha et al., 2005; Thoma et al., 2005; Scheidl et al., 2008; Ewing et al., 2010; DeLong et al., 2012; Oskin et al., 2012; Duffy et al., 2013). Furthermore, for some applications airborne LiDAR may not provide sufficient spatial resolution. For example, point spacings of tens of centimeters, densities typical of modern airborne LiDAR data sets, may not adequately characterize small geomorphic offsets, discrete fault scarps, or intricate aspects of fault scarp erosion (Arrowsmith and Rhodes, 1994; Elliott et al., 2011; Haddad et al., 2012), and in multitemporal mode are unlikely to capture displacements of a few centimeters (e.g., Borsa and Minster, 2012; Nissen et al., 2012), such as those expected from fault creep or postseismic afterslip.

Terrestrial LiDAR, also known as terrestrial laser scanning (TLS) or tripod LiDAR, uses portable scanners that are set atop surveying tripods while they record data (Fig. 1B). If necessary, scanners are moved to new positions in order to capture targets from optimal viewing angles and to avoid occlusion (i.e., from vegetation). The need to move equipment introduces time demands that typically limit terrestrial LiDAR data acquisition to site dimensions of up to a few hundred meters. However, the scanners are compact and can be carried to remote locations, overcoming a major limitation of airborne LiDAR (though with power sources also required, the equipment can become cumbersome). These capabilities of terrestrial LiDAR have led to its extensive use as a deformation monitoring tool, particularly for landslides, debris flows, and rockfalls (for a review, see Jaboyedoff et al., 2012). In tectonics research,

it has also been used to monitor fault creep (Wilkinson et al., 2010; Karabacak et al., 2011), fault scarp degradation (Elliott et al., 2011; Haddad et al., 2012), and postseismic river knickpoint retreat (Cook, 2013), as well as to characterize offset channel systems (Gold et al., 2011).

Terrestrial LiDAR can record multiple returns, allowing most vegetation to be filtered from the scene, much like in airborne surveys. These terrestrial surveys are conducted from closer distances to the target site than aerial mapping methods, and can therefore produce denser point clouds (ten to thousands of points per square meter) and thus higher resolution DEMs than typical for airborne LiDAR. However, these densities also tend to be more spatially variable, depending as they do on the local surface aspect with respect to the scanner. Thus, terrestrial LiDAR can achieve better results for near-vertical features, and has been particularly useful as a way to characterize fault scarps (e.g., Haddad et al., 2012; Gold et al., 2013). As a tradeoff, it is more difficult to comprehensively cover undulating landscapes because of data gaps in the shadow zones where terrain is out of the scanner's line of sight. Although the advent of mobile platforms offers a potential solution to such data gaps (Brooks et al., 2013), the cost of a portable LiDAR system remains prohibitive for many researchers; the least expensive units capable of terrain mapping cost several tens of thousands of dollars.

SfM

SfM offers an alternative method of producing high-resolution digital topographic data that overcomes many of the limitations of airborne or terrestrial LiDAR. This mapping technique builds upon traditional stereophotogrammetry by producing digital three-dimensional (3D) models of a scene using a collection of photographs with overlapping coverage and changing perspective (Fig. 1C). Like traditional photogrammetry, SfM triangulates among the locations of individual features matched in multiple images to build the geometry of the scene. Unlike traditional photogrammetry, SfM algorithms support large changes in camera perspective and photograph scale through use of a feature recognition algorithm (Scale Invariant Feature Transform; Lowe, 2004; Snavely et al., 2008), which eliminates the need for grid-like image acquisition and makes the technique easy to implement. Because each matched feature is colored, the scene texture as a set of red-green-blue (RGB) values is easily coregistered with its geometry. This is an improvement upon some LiDAR surveys, for which a return "intensity" is often the only record of scene texture. SfM requires only a consumer grade camera, and readily available commercial or open source software, such as Agisoft Photoscan, Bundler Photogrammetry Package, PhotoModeler, or Microsoft Photosynth.

Originally used to visualize urban settings (e.g., Snavely et al., 2008), SfM has recently been adopted by Earth scientists as an affordable means of mapping natural landscapes, initially using ground-based photosets. Because SfM cannot collect multiple returns, it cannot "see through" canopy in the manner that LiDAR can, and acquiring a good ground model in areas of dense vegetation will consequently be challenging. So far, the use of SfM for terrain mapping has been limited to sites with sparse or low-lying vegetation. In addition, it has so far been limited to target areas with dimensions to a few hundred meters, similar in size to those typically mapped with terrestrial LiDAR, but much smaller than most airborne LiDAR surveys.

Westoby et al. (2012) generated SfM models constructed from ground photos at three field sites of varying surface cover and topographic complexity: a steep coastal hillside, a glacial moraine, and a bedrock ridge. At the first site, they obtained SfM point cloud densities of up to a few hundred points per square meter, somewhat lower than those of an overlapping terrestrial LiDAR data set, which in places exceeded 1000 points/m^2. Elevation differences determined by subtracting an SfM-derived DEM from the LiDAR DEM were mostly (86%) <0.5 m. James and Robson (2012) also used ground photographs, taken at close range (20 m), to produce a time series of seven SfM models of coastal cliffs over the period of one year. These models achieved point cloud densities of several thousand points per square meter with discrepancies of up to a few centimeters compared to a model constructed from a coincident terrestrial LiDAR scan. The SfM data were accurate enough to clearly image cliff retreat between successive surveys. In the same paper, SfM was used to construct a 3D model of a volcanic crater from photographs captured from a piloted aircraft flying 1000 m above ground level (AGL), obtaining a point cloud density of ~2 points/m^2. Comparisons with a DEM constructed from traditional photogrammetry showed general agreement at the 1 m level, but a few patches with differences of as much as 2 m. These results illustrate the trade-off between camera-target distance and model precision and resolution.

Incorporation of Low-Cost Aerial Platforms

The past few years have seen a marked increase in the use of small UAVs and other unmanned aerial platforms for scientific remote sensing or photogrammetry studies (e.g., Hugenholtz et al., 2012), offering clear potential advantages for the collection of SfM imagery. The low-altitude flight capabilities of commercially available UAVs (typically a few tens of meters AGL) increases terrain detail, thus improving the resolution of SfM data, albeit at the expense of spatial coverage (particularly compared to airborne LiDAR). These systems can cost as little as a few hundred dollars, making them readily accessible to many geoscientists. Larger UAV platforms require flying permits in some countries (Hugenholtz et al., 2012), but the use of tethered platforms like helium balloons and blimps can avoid these issues.

A few recent SfM or close-range photogrammetric studies have incorporated this technology in the form of multirotor helicopters (Harwin and Lucieer, 2012; Niethammer et al., 2012; Rosnell and Honkavaara, 2012; Turner et al., 2012), fixed wing planes (d'Oleire-Oltmanns et al., 2012), and helium-filled blimps (Fonstad et al., 2013). The camera is attached to the underside of the platform, pointing downward, and collects photographs at a user-specified time-lapse interval or through remote-controlled triggering, resulting in expedited data collection from an advantageous viewing geometry. This strategy produces a relatively even spatial distribution of points compared to ground-based SfM, which can have the same line-of-sight issues as terrestrial LiDAR (e.g., Westoby et al., 2012). Harwin and Lucieer (2012) generated an SfM point cloud with several hundred points per square meter of a coastal site in Australia, using photographs collected from a multirotor helicopter flying ~40 m AGL and incorporating differential GPS ground control points. Comparing their SfM point cloud to a total station survey, they estimated the SfM data to be accurate to <4 cm. Fonstad et al. (2013) made a comparison between SfM data, generated using photographs taken from a helium blimp at a height of ~40 m, and conventional airborne LiDAR at a site on a bedrock channel and floodplain in Texas. Their SfM point cloud density was ~10 points/m^2 compared to just 0.33 points/m^2 for the airborne LiDAR. They found significant discrepancies in height values, averaging 0.6 m across the scene, attributing the largest errors to a region with many rocks and trees.

AFFORDABLE STRUCTURE FROM MOTION MAPPING SYSTEM

Here we outline an SfM workflow designed for mapping fault zone topography but also suitable for many other applications with similar requirements. A key goal is to find an appropriate balance between the affordability and acces-

sibility of the system (its cost, ease, and speed of use) and the quality of the resulting topographic data (accuracy and density). As a result, our methodology differs somewhat from the procedures followed in the SfM studies described previously (Fig. 2). In particular, we designed our approach to be easily completed by a person working alone, or in situations where data collection and processing must be expedited, such as field mapping after an earthquake. In the following we discuss our choice of platform and strategy for photograph collection and our preferred way of processing this imagery and generating topography. We demonstrate our complete workflow at two field sites on major faults in southern California and assess the accuracy of our SfM point clouds against colocated LiDAR data.

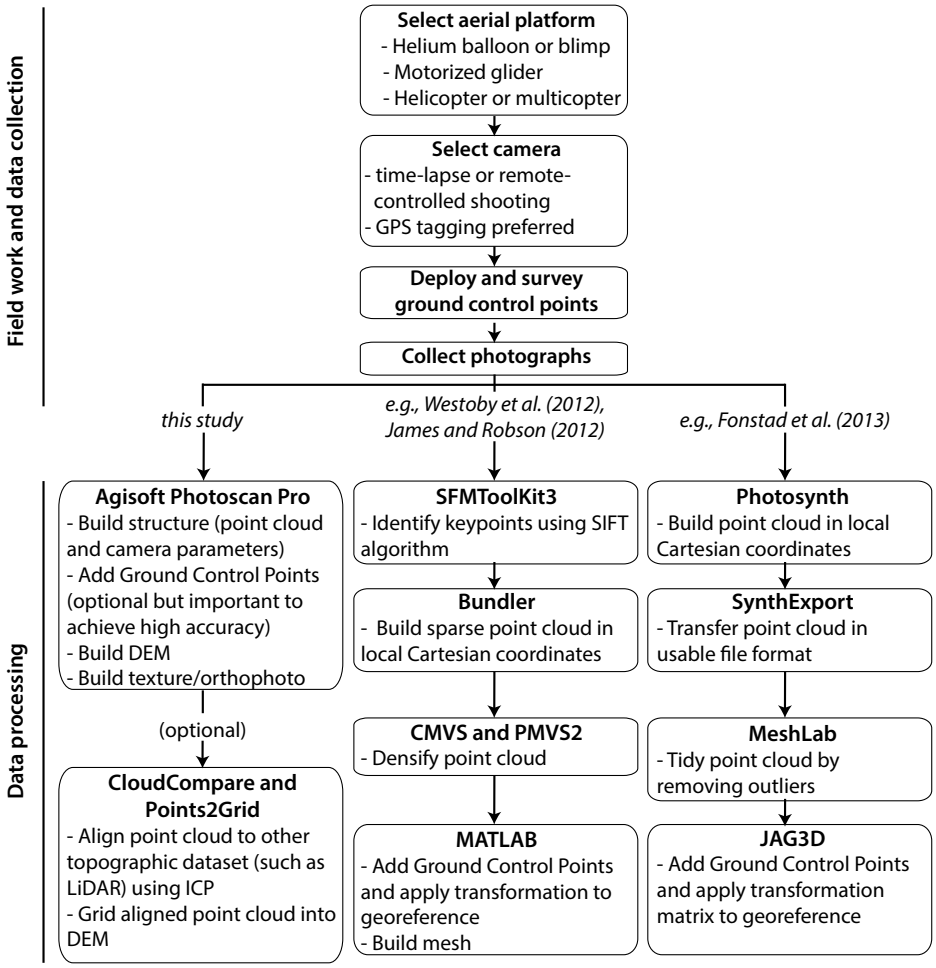

Figure 2. A summary of the workflow presented in this paper, separated into field work and data collection (top) and data processing (bottom). In the data processing, our workflow is shown on the left and two alternative published procedures are shown to the right. GPS—global positioning system; DEM—digital elevation model; ICP—iterative closest point.

Field Work and Data Collection

We chose to use a radio-controlled motorized glider (McGarey and Saripalli, 2013) and a tethered helium balloon as camera platforms, both easily deployed by a single person and relatively affordable, costing a few hundred dollars in total. The motorized glider (Fig. 3A) can cover larger areas more quickly, but requires more experience to control remotely. However, a skilled pilot does have control over the platform position and camera angle. Like many other UAVs, the glider also has the potential to be programmed to fly along a preset route that requires little interference by the operator. Our glider was purchased as a kit from Electric Flights and assembled in a few hours. After hand launching, the glider is operated using a 2.4 GHz Spektrum DX6i Transmitter and Spektrum 6100e Park Receiver and powered with a single 3000 mAh 4 Cell 14.8V lithium polymer battery, giving a flight time of ~20 min. The glider carries a lightweight Canon PowerShot SX230 HS (high sensitivity) camera, which has a 5 mm focal length, 12 megapixel resolution, and internal GPS. Interval shooting can be triggered at a specified delay time by programming the SD card with the freely available Canon Hack Development Kit.

The helium balloon (Figs. 3B–3D) offers the advantage of simplicity. In moderate wind speeds, a single person can pull the tethered platform across the target area, although having a second person expedites setup and can improve the efficiency at which the survey area is covered, particularly in blustery conditions. Our balloon inflates to ~4 m^3 and carries a harness (a Brooxes picavet) from which we attached a downward-pointing, 16 megapixel-resolution Nikon D5100 camera with an 11 mm Toshiba lens and a connected Easytag GPS tagger. The total weight of the camera, lens, and GPS tagger is ~1 kg. The balloon is tethered using a lightweight kite string and reel. The camera is set to interval shooting mode and the delay between shots is specified in the camera menu (typically 5–10 s, chosen to ensure plentiful overlap between photographs). We set the focus to infinity and choose an appropriate (fixed) exposure setting depending on the ambient light conditions.

The strategy for photograph collection depends on the shape and size of the target area, as well as the desired resolution of the topographic data. We find that a single pass of the balloon or glider is sufficient to capture small-scale topography along thin, sublinear targets such as the Landers earthquake rupture, where the area of interest is narrower than the width of a single photograph footprint. "Lawn mower" acquisition patterns, which cover a site with a series of subparallel flight paths, are effective at covering wider targets, as we demonstrate at the Washington Street site (San Andreas fault). Given sufficient photograph overlap, data resolution is determined by the height of the platform. The length and weight of our kite string limited the balloon to an elevation of ~120 m AGL (at close to sea level), while the glider can fly at a few hundred meters above ground level. When photographs are taken closer to the ground, SfM point cloud density and DEM resolution improve at the expense of smaller photograph footprint size and overlap, with a resulting increase in the time taken to survey a given area. We explore these trade-offs with photosets collected at a range of heights in the discussion of the Washington Street Site.

Data Processing

We build the SfM point clouds and DEMs using the commercial Photoscan Pro software made by Agisoft LLC (herein called Photoscan).

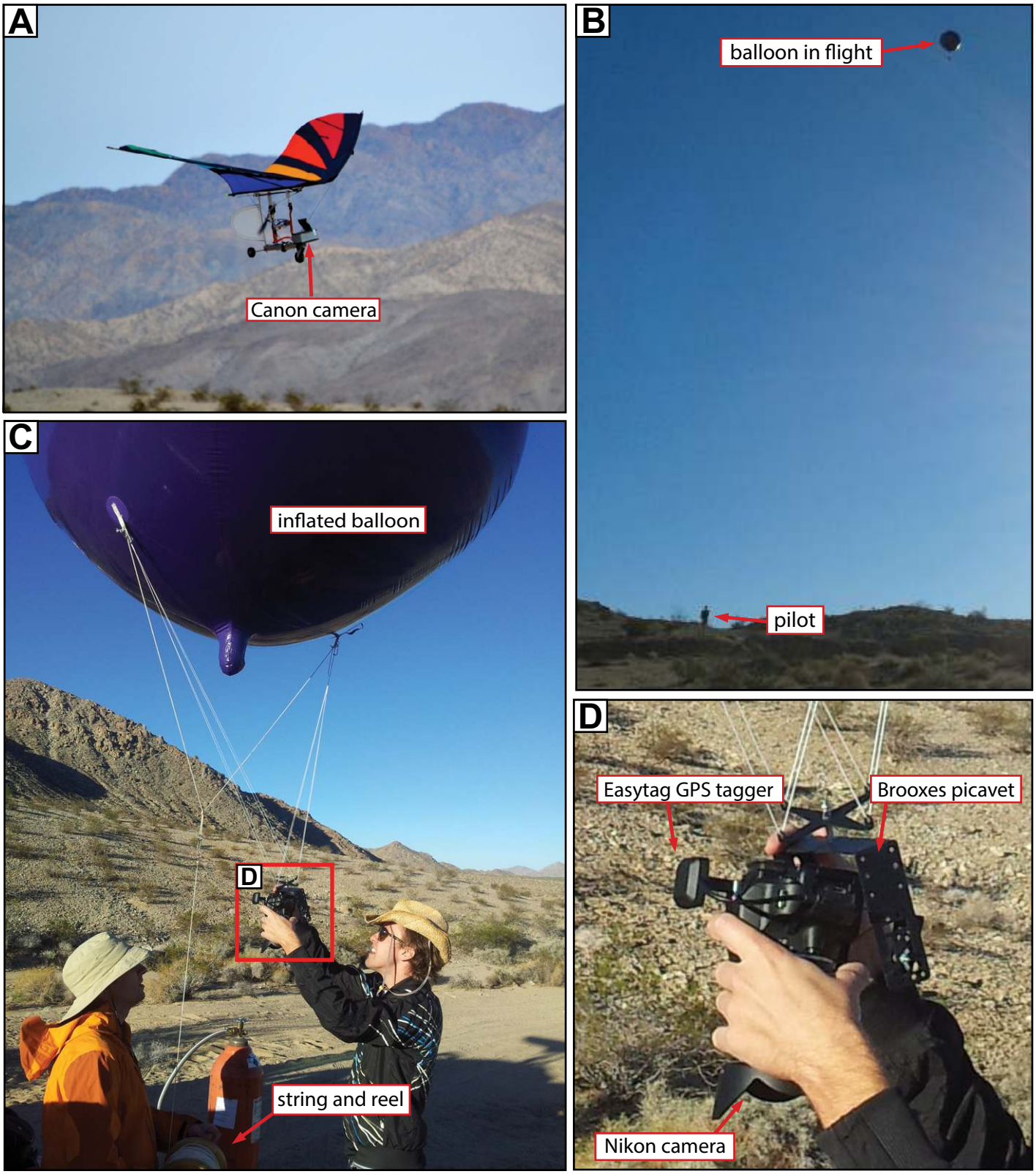

Figure 3. Photographs showing the two camera platforms discussed in this paper. (A) Motorized glider in flight. (B) Helium balloon in flight with pilot for scale. (C) Balloon in preparation. (D) Close-up of camera and harness (picavet). GPS—global positioning system.

We choose this software for its two principle advantages over other published procedures (Fig. 2). First, Photoscan is able to implement camera GPS positions into the SfM calculations as opposed to relying entirely on ground control points (GCPs) for scene georeferencing, as the other workflows do. Using these initial position estimates expedites the scene reconstruction. Second, Photoscan can do all of the steps in the processing chain, whereas the other approaches rely on several separate programs to build a final georeferenced model (Fig. 2).

The highly automated Photoscan workflow generates topography and texture from a photoset in four main steps; for a more complete description of this workflow and some of the algortihms employed, see Verhoeven (2011). (1) The photographs are loaded, including their tagged GPS positions if available. Usually, these are stored in the EXIF (exchangeable image file format) metadata of each JPEG along with certain other camera parameters and are easily loaded into Photoscan. (2) Matching features are automatically identified and the scene structure (camera positions and orientations and colored point cloud) is constructed. At this stage, the point cloud can be exported in ASCII or LAS formats and in a user specified coordinate system. (3) A DEM is constructed from the point cloud by fitting polygons to points that characterize a facet of the ground surface. This mesh can also be exported in a variety of common formats and coordinate systems. (4) An orthorectified composite photograph is generated.

In practice, some guidance by the user is required. In step 1, we quality check the photos, discarding those that are blurry or dominated by sky (this can occur during glider flights when the aircraft banks). Steps 2 and 3 are automated processes guided by user-specified accuracy and quality options. Step 2 can be completed at three levels of accuracy that trade off against processing time. While still at the survey site, we run this step at the lowest setting on a field laptop in order to check that we have complete photograph coverage, but for the final point clouds presented in this study we choose the highest level possible. Photoscan can interactively tidy the point cloud by removing poorly constrained points that have high reprojection or reconstruction errors or mismatched points that are far from the surface. This step is not required, but it improves the point cloud by filtering erroneous points and leaving only those that represent a continuous surface; it can also make subsequent gridding considerably quicker.

Step 3, building the geometry, or mesh, that characterizes the topography, can be completed at five quality levels, with processing time increasing significantly at each level of improvement. Here, the word "quality" has no implications for accuracy of the point cloud, but instead refers to resolution. When the highest level of quality is selected, the model is built using the densest possible point cloud, which exploits the original photographs at full resolution; for each step reduction in quality setting, the density of the sourced point cloud decreases by a factor of two, as downsized versions of the photographs are used. This step can be further expedited outside of Photoscan by using alternative programs to generate the DEM; we used GEON points2 grid (Kim et al., 2006), which computes at each grid node the minimum, maximum, mean, or inverse distance weighted mean value of points within a user-specified search radius. This requires more interaction from the user, but is less time and graphics processor intensive than step 3 in Photoscan and avoids certain artifacts.

As the number of photos used to build the point cloud increases, the time required for Photoscan to complete these steps grows significantly. When using low-quality settings on tens of photos, Photoscan can complete the workflow in minutes, while high-quality settings on hundreds of photos can take as long as a few days. Processing time is expedited by using a powerful computer with a large random access memory (RAM), multiple cores, and a high-quality graphics card. Here, we use an eight-core Intel 7 processor with 32 GB RAM and an Nvidia GeForce 670 graphics card. Similarly, point cloud file sizes scale upward with quality settings, as do export times. For this reason we choose to primarily work with point clouds generated at the low-quality setting: those downsampled by a factor of eight. This preference holds for the analyses performed throughout this work; however, our DEMs are gridded using denser point clouds (respective qualities for each site and test are identified in following discussions).

A few additional steps are required to register the grids if very accurate geospatial coordinates are desired. As mentioned earlier, the SfM data are initially georeferenced using the instantaneous coordinates of the camera's GPS that are stamped to the metadata of each picture. This capability significantly decreases the processing time as an automated part of the photo alignment stage, and eliminates the time spent deploying and/or identifying GCPs. However, errors in the camera GPS location can lead to shifting, tilting, or warping (bending, stretching, and shrinking) of the resulting topographic data, as we demonstrate in the following SfM data assessment. For applications in which such distortions are a significant hindrance, the user must incorporate independently located GCPs. In this case, the user assigns coordinates to a few evenly distributed features within the scene, and Photoscan optimizes the point cloud to better fit these new constraints. In the SfM data for our two test sites, we use GCPs surveyed through differential GPS or prominent natural features that are easily identifiable in existing LiDAR data.

SfM DATA ASSESSMENT AT TWO TEST SITES

Previous studies had mixed results when comparing SfM and LiDAR data sets (James and Robson, 2012; Westoby et al., 2012; Fonstad et al., 2013). Here, we demonstrate our SfM mapping system at two field sites, and assess the accuracy by comparing our data sets to existing airborne or terrestrial LiDAR. We use two steps to compare the pairs of data sets, both implemented in the open source software CloudCompare (http://www.danielgm.net/cc/).

1. We apply the iterative closest point algorithm (ICP) to achieve a global alignment of the SfM point cloud with the reference LiDAR point cloud (Chen and Medioni, 1992; Besl and McKay, 1992). ICP works iteratively to find the rigid body transformation (translation and rotation) that minimizes closest point pair distances between clouds. This step helps account for remaining differences in the global registration of the two data sets that result from changes in absolute GPS positioning between the two surveys, but does not affect the internal shape of either data set.

2. Having applied the global ICP transformation, cloud to cloud distances can be measured independent of these registration differences, which therefore only reflect discrepancies in the internal shape of each point cloud. For each point in the reference LiDAR point cloud, we locate the nearest point in the transformed SfM cloud and measure the vertical component of the Euclidian distance between the two. We choose to measure this distance at each LiDAR point, rather than at each SfM point, based on the lower density of the LiDAR points; this configuration ensures smaller distances between each pair of compared points.

We demonstrate our workflow at two field sites in southern California (Fig. 4). The Washington Street site covers a small portion of the Banning strand of the southern San Andreas fault. Here we compare the SfM topography with the B4 airborne LiDAR survey (Bevis et al., 2005), a rich data set collected in May 2005 that led to the identification and characterization of hundreds of geomorphic offsets along the southern San Andreas fault (Zielke et al., 2010, 2012; Madden et al., 2013) as well as the central San Jacinto fault (Salisbury et al.,

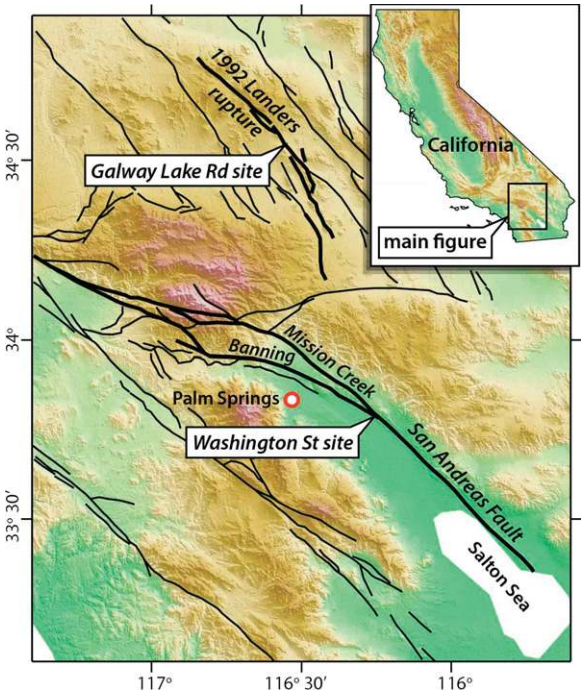

Figure 4. Quaternary fault map of southern California showing locations of the Washington Street and Galway Lake Road (see inset for location of main map). Faults are from the U.S. Geological Survey Faults and Folds database (Haller et al., 2004). The San Andreas fault and Landers earthquake rupture are highlighted in bold. The Washington Street site is on the Banning strand of the San Andreas fault, ~2 km southwest of the Mission Creek strand and ~8 km northwest of where these two strands merge.

2012). The Galway Lake Road site (Arrowsmith and Rhodes, 1994) covers a short segment of the 1992 Landers earthquake surface rupture on the Emerson fault. We compare the SfM topography to a local terrestrial LiDAR data set collected in 2009 (details in Haddad et al., 2012). The aim of our survey at this location was to test its suitability for mapping sublinear ruptures at short notice, such as in response to an earthquake. Our SfM topography data sets are freely available for download from the OpenTopography portal (www.opentopography.org).

Results: Washington Street Site, San Andreas Fault

The Washington Street site, centered at 33°48′58″N, 116°18′40″W, covers a small section of the southern Banning strand of the San Andreas fault, along the southwestern margin of the Indio Hills east of Palm Springs, California (Fig. 4). Neither this fault nor the northern Mission Creek strand have ruptured historically, contributing to the uncertainty in how the slip accommodated along the San Andreas fault is partitioned between these two subparallel structures (e.g., Fumal et al., 2002). At the target site, the Banning fault strand crosses a sparsely vegetated Quaternary alluvial fan incised by an active channel.

We collected more than 1000 photographs of the Washington Street site covering an ~300 × 300 m area (~0.1 km^2) using both the helium balloon and motorized glider as camera platforms. Data collection, including system assembly and disassembly, took <2 h for each platform. We selected ~800 usable photos captured from the balloon at 3 different heights: 50 m AGL, 100 m AGL, and ~120 m AGL. For each height, we pulled the balloon at walking pace along a lawnmower pattern path where each line intersected the fault at a nearly perpendicular angle. The Nikon D5100 camera shot interval was set to 5 s. In addition, we took 107 photos from the glider flying at heights of 150–300 m AGL and at speeds of 7–10 m/s, covering an area ~4 times the size of that mapped with the lowest-flying balloon. The glider's Canon PowerShot SX230 HS camera was programmed to capture photographs at a 5 s interval, which provided good photo coverage at these elevations and velocities.

Following photo collection and selection, we loaded and processed each set of photos independently in Photoscan, in order to compare results for different platform heights, collection strategies, and processing settings. Table 1 lists the results for each of the Washington Street site SfM photosets, as well as details of the B4 LiDAR data for comparison. For each balloon photoset, we initially built the DEMs at the medium-quality setting, but for the higher elevation glider photoset (150–300 m AGL) we used the high-quality setting. Although increasing the height of the balloon enabled wider ground footprints of each photo (and therefore quicker coverage of the entire site), the resulting point cloud density suffered; for example, doubling the height of the balloon decreased the point cloud density by >50%. We also produced a DEM at the best available (ultrahigh) quality setting for the low-altitude balloon photoset to observe how this alters the resolution. The resulting 3 cm resolution of the DEM is more than 3 times finer than that of the medium-quality DEM constructed from the same photoset, but took considerably longer (several days, as opposed to several hours) to build.

SfM results at the ultrahigh-quality setting are shown in Figures 5A (DEM draped with orthophoto) and 6A (DEM). At the low-quality setting, 50% of the SfM point cloud contains >700 points/m^2 and 90% contains >60 points/m^2, making the point cloud significantly denser than that of the airborne LiDAR (Figs. 5B, 5C). SfM point densities generated at the ultrahigh-quality setting are eight times higher. SfM point density increases with photo coverage (Fig. 6B), and is therefore highest in the central region of the scene and lower around the edges. At such high density, the structure of the site is evident in the SfM point cloud even at very close range (Fig. 5B, inset). Furthermore, each point in the cloud is colored with RGB values, an improvement upon airborne LiDAR in which often only a return intensity is recorded. This color information could potentially be useful for stripping vegetation from the scene (in this case bushes, which appear as dark lumps contrasting with the lighter alluvium), perhaps using an adaptation of

TABLE 1. SUMMARY OF PHOTOSETS AND TOPOGRAPHIC DATASETS FROM THE WASHINGTON STREET SITE, SAN ANDREAS FAULT

Dataset type	Platform	Flying altitude (m)	Number of photos	Point cloud density (low-quality setting, points/m^2)		DEM build quality	DEM pixel dimension (cm)
				90%	50%		
SfM	Balloon	50	233	>60	>700	Medium	10
SfM	Balloon	100	273	>20	>205	Medium	20
SfM	Balloon	~120	244	>8	>125	Medium	27
SfM	Balloon	50	233	>60	>700	Ultrahigh	3
SfM	Glider	150–300	107	>2	>15	High	11
Airborne lidar	Airplane	600	N/A	>1	>1.75	N/A	50

Note: SfM—structure from motion. Table compares the effect of platform height and DEM (digital elevation model) build quality on the resulting point cloud density and DEM resolution. The last line describes the B4 airborne lidar (light detection and ranging) survey (Bevis et al., 2005). N/A—Not applicable.

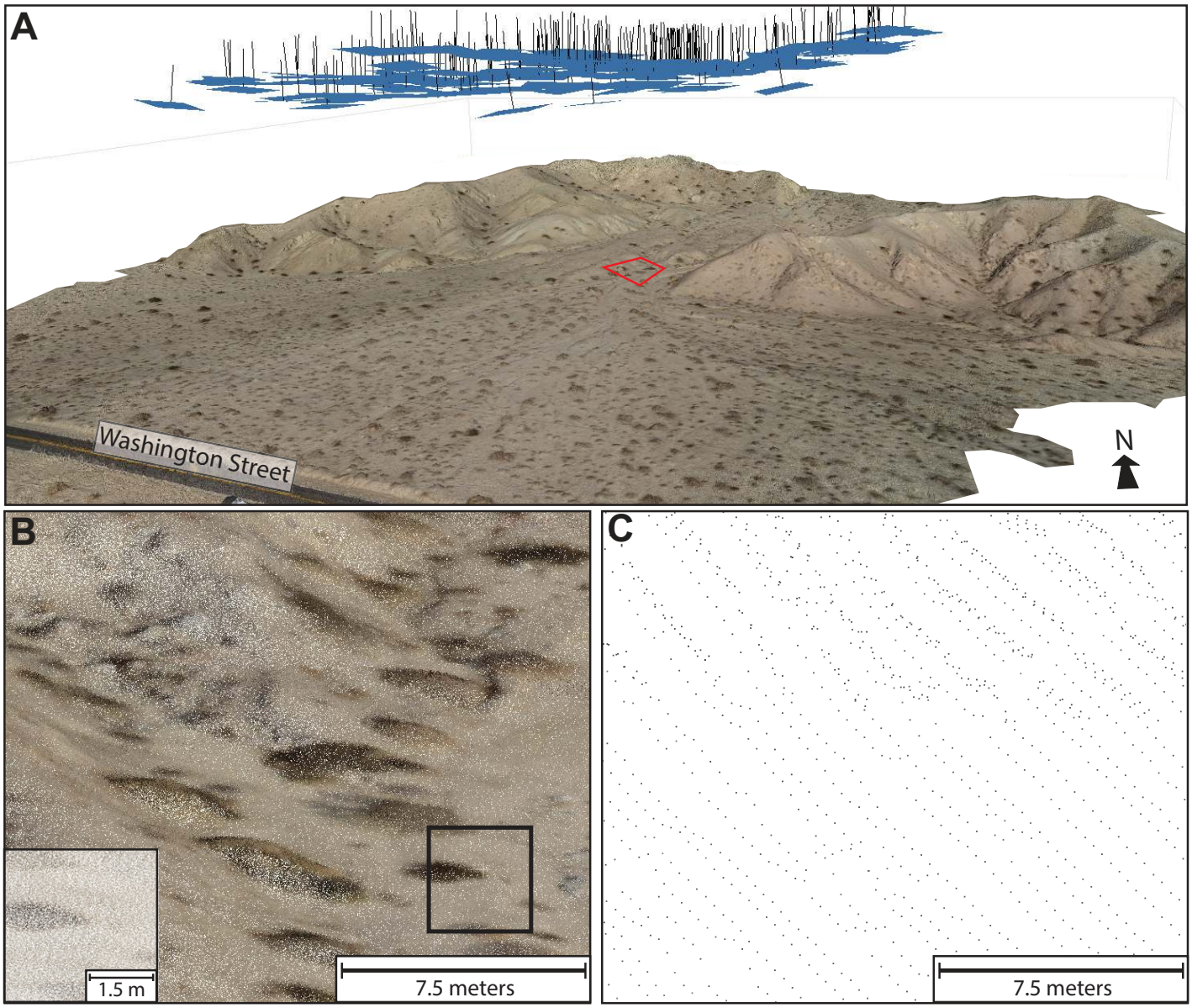

Figure 5. (A) Perspective view of the final Photoscan digital elevation model and draped orthophoto from the Washington Street site (San Andreas fault). Camera positions are shown as blue rectangles and the normal to each photograph is marked by a black line. (B) A close-up view of the low-quality structure from motion point cloud (several hundred points/m^2) inside the red polygon in A. At greater magnification (inset), the individual colored points are visible. (C) The B4 airborne LiDAR (light detection and ranging) point cloud (2–4 points/m^2) in the same region as B, colored by intensity and clearly showing the individual scan lines of the survey (Bevis et al., 2005).

the method by Wang and Glenn (2009), which removes canopy returns from airborne LiDAR point clouds by filtering intensity values.

A comparison of the 3-cm-resolution SfM DEM to the B4 airborne LiDAR DEM gridded at 0.5 m resolution is shown in Figures 6C and 6D. At this magnification, the LiDAR DEM appears pixilated and in this locality it also shows a striped "corduroy" pattern (i.e. parallel stripes), an artifact common to airborne LiDAR data due to misaligned overlapping flight lines. The SfM DEM reveals centimeter-scale details that do not stand out in the airborne LiDAR DEM due to its lower resolution and corduroy pattern. Airborne LiDAR surveys now achieve significantly higher point cloud densities than the B4 survey did (>10 points/m^2 compared to 2–4 points/m^2), but even these would appear pixilated in comparison to the SfM data at the magnification shown here. Nevertheless, for many tectonic applications the point densities achieved by airborne LiDAR are more than sufficient, and these problems are offset by the large areas (to hundreds of square kilometers) mapped in these surveys, which could not feasibly be covered with our SfM system.

When the geometry and resulting DEM is built at lower qualities, we find that Photoscan fits the point cloud surface with large, sharp polygons (Fig. 7A). Although the resolution of the DEM is nominally 10 cm, fine details of the geomorphology are badly obscured by these artifacts. This is an issue with the gridding of the DEM rather than with the point cloud, and alternative gridding software generated much smoother results using the same point cloud data (Fig. 7B).

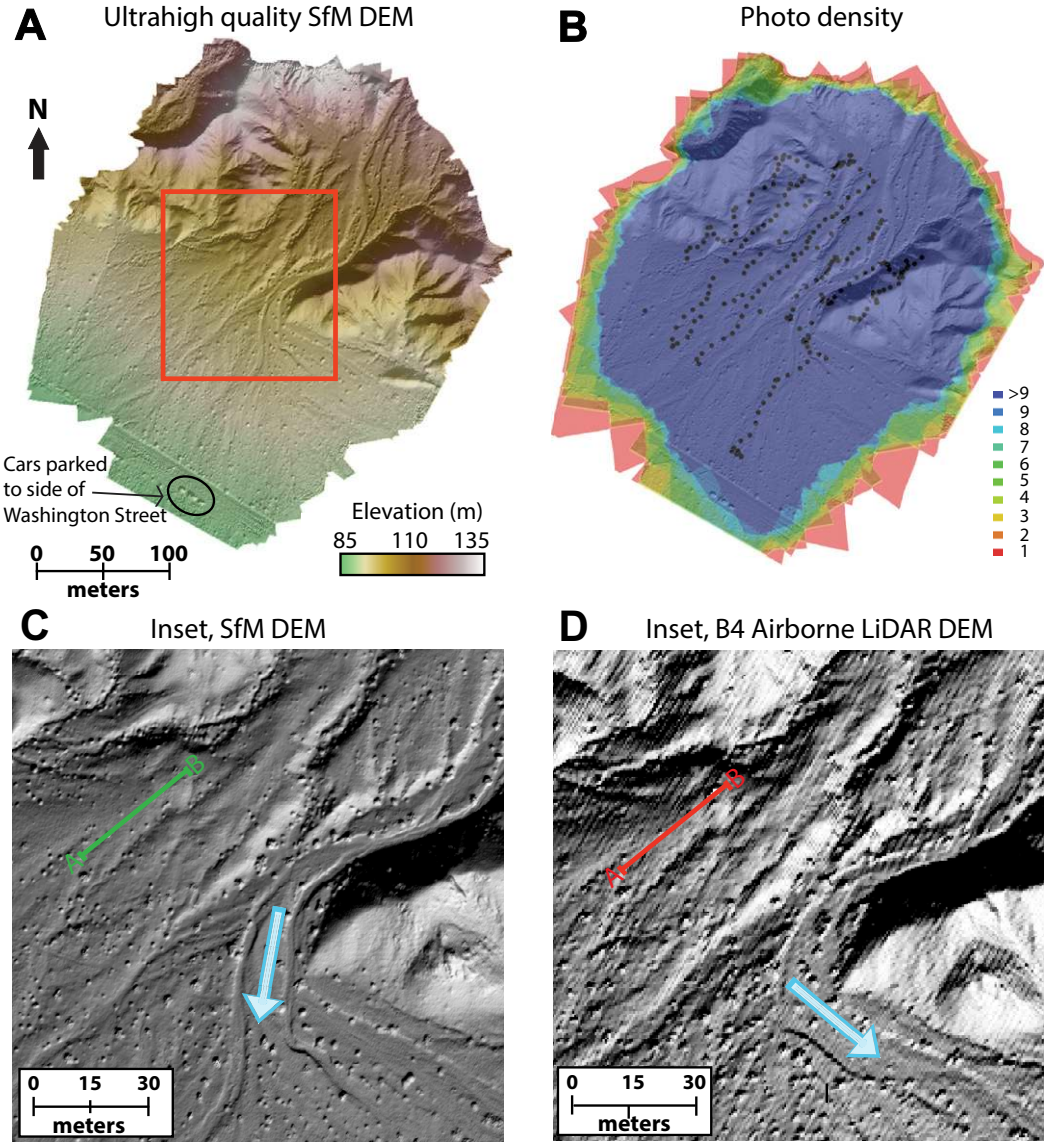

Figure 6. (A) Washington Street site (San Andreas fault) structure from motion (SfM) ultrahigh-quality digital elevation model (DEM) produced with the photoset collected by the helium balloon at 50 m above ground level, artificially illuminated from azimuth 155°, elevation 21°. (B) Density map of photograph footprints for the same survey. Black dots show the camera location at the time of each photo. (C) Boxed region of SfM DEM shown in A. The blue arrow shows the path of the main channel in 2013. The green line shows the location of the cross-scarp profile in Figure 9. (D) B4 airborne LiDAR (light detection and ranging) DEM over the same area (Bevis et al., 2005). The DEM was generated from the raw point cloud using the GEON points2 grid (Kim et al., 2006), taking the inverse distance weighted value at 0.5 m node spacing and using a search radius of 0.8 m. The red line shows the location of the cross-scarp profile in Figure 9. Note the difference in channel flow path when the LiDAR data set was acquired in 2005 (blue arrow).

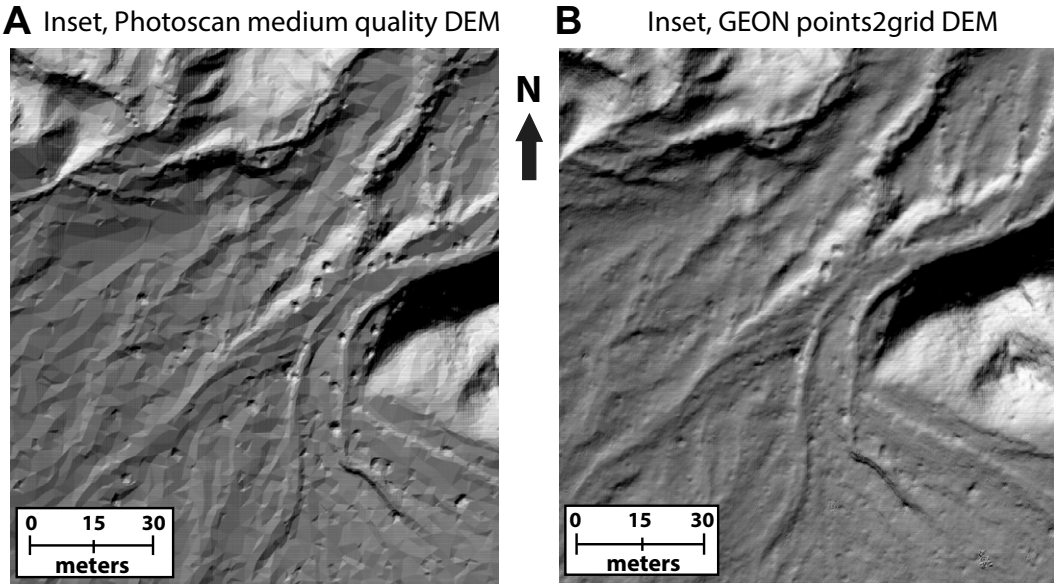

Figure 7. (A) Structure from motion (SfM) digital elevation model (DEM) of the Washington Street site (San Andreas fault) built in Photoscan at the medium-quality setting shows polygonal artifacts. The extents of this figure are the same as in Figures 6C and 6D. (B) SfM DEM built from the same Photoscan point cloud but now gridded with GEON points2grid (Kim et al., 2006), removing the polygonal artifacts. After experimentation, a 0.08 m node spacing with a 0.10 m search radius and inverse distance weighting allowed us to achieve fine detail without leaving holes.

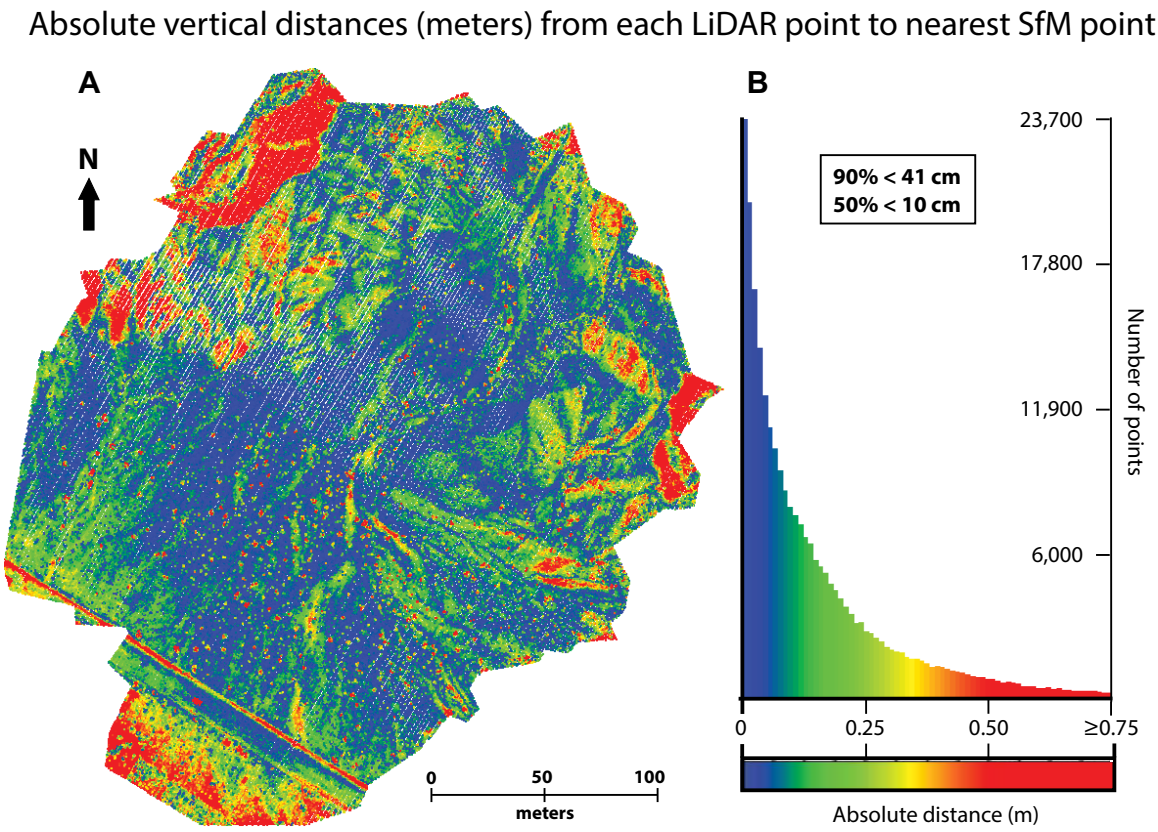

Figure 8. Comparison between airborne LiDAR (light detection and ranging) point cloud and the structure from motion (SfM) point cloud built at the low-quality setting without ground control points for the Washington Street site (San Andreas fault). (A) Vertical distances between each LiDAR point and its closest SfM neighbor. (B) A histogram showing the spread in these values across the entire scene. The color scale is the same in both map and histogram, and saturates at 0.5 m to better capture the variation at small distances. The comparison reveals that most of these distances are <10 cm.

Assessing SfM Accuracy without GCPs

Initially, we compare the alignment of the SfM topography with the B4 airborne LiDAR data set using the ICP alignment and cloud to cloud distance computation (described at the beginning of the SfM data assessment discussion). For this first comparison, we do not use GCPs, and our SfM data set is georeferenced using only the camera GPS points and lens metadata stamped to each JPEG. In this instance, all ICP translational components were on the order of meters, reflecting a significant mismatch in the GPS registration of the two surveys. All rotational components were ~0.01 radians, values that reflect tilting of the SfM data set. For some applications this is an important point, because without an alternative (LiDAR) data set, registration errors would produce residual slope errors in the SfM point cloud.

Results of the cloud to cloud distance computation (after global registration) show that 50% of the LiDAR points deviate vertically from the closest SfM point by <10 cm and 90% by <41 cm (Fig. 8). The largest deviations are observed in four types of areas: (1) steep slopes, (2) outer edges of the difference map, (3) large bushes, and (4) active or recently active stream channels. In the case of steep terrain, it is unclear whether the deviations result from errors in SfM point positioning, or from uncertainties in LiDAR heights, which increase on steep slopes due to the larger footprint of the steeply inclined laser beam (Spaete et al., 2011). Higher deviations around the outer edges of the difference map are likely to be primarily caused by errors in SfM point positions, as these were reconstructed using fewer photographs from a smaller range of look angles than data in the central part of the scene. Bushes, many of which appear as red dots in the difference map, may have grown, died, or otherwise changed between the 2005 LiDAR survey and the 2013 SfM survey. These deviations might also reflect partial penetration of shrubs by LiDAR. The stream channel switched its primary course during the 8 yr period between surveys (Figs. 6C, 6D) such that both the old and new stream channels have undergone some erosion or deposition, which is reflected in the difference map. A final, but minor, discrepancy between the two data sets results from the mapping of a passing car by the airborne LiDAR survey and the inclusion of our parked field vehicles parked in the SfM data set.

Despite the small vertical cloud to cloud distances, the magnitudes of the rotational components of the ICP alignment matrix determined in CloudCompare indicate that our SfM point cloud is tilted compared to the airborne LiDAR. We visualize the extent of this tilting by comparing a cross-scarp profile from the SfM DEM to the same profile through the airborne LiDAR DEM (Fig. 9; profile locations shown in Figs. 6C, 6D). This analysis confirms that the SfM data set was tilted before the global ICP transformation was applied, resulting in a steeper apparent slope and slightly larger apparent vertical displacement across the scarp than actually exists.

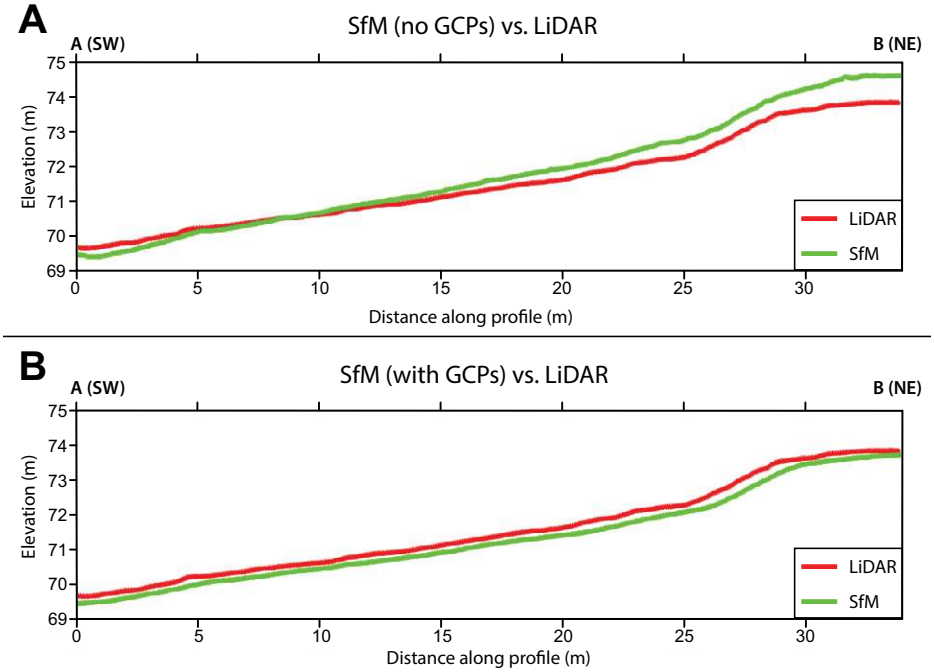

Figure 9. Topographic profile crossing the Washington Street site (San Andreas fault) fault scarp in the location indicated in Figures 6C (green line) and 6D (red line). (A) Structure from motion (SfM) digital elevation model (DEM) without ground control points (GCPs; green) is compared to the B4 airborne LiDAR (light detection and ranging) DEM (red). (B) Same as panel A, but the green line now corresponds to the SfM DEM optimized with GCPs. This comparison shows that although the absolute location of the GCP-optimized SfM DEM differs from that of the airborne LiDAR by ~1 m (presumably reflecting slight differences in GPS base stations), the tilting of the SfM topography observed in A has been removed.

Assessing SfM Accuracy with GCPs

For some tectonic applications of high-resolution topography, such as scarp degradation modeling (e.g., Nash, 1980; Hanks et al., 1984) and monitoring (Elliott et al., 2011; Kogan and Bendick, 2011), and hillslope and drainage network analysis (e.g., Hilley and Arrowsmith, 2008; Hurst et al., 2013), these errors in slope could compromise the quantitative analysis of the landscape. We therefore investigated whether providing Photoscan with a few precisely located GCPs as additional constraints can eliminate tilting and other distortions from the SfM topography. This test helps establish our confidence in SfM topography in areas where no LiDAR data exist and where comparisons like those in Figures 8–10 are impossible, but GCPs can be used.

First, we produced a modified SfM point cloud optimized in Photoscan using nine GCPs. These were sourced from a set of differential GPS transects, which follow several features within the central portion of the Washington Street site. The transects were collected with a Trimble GeoXH handheld GPS in January 2013, and were postprocessed with local base stations to produce absolute uncertainties of ~20 cm. The GPS data were overlain on an aerial photograph, which was easy to correlate with the SfM orthophoto. We identified features distinguishable in both images that corresponded to points on the GPS transect, and marked their locations (easting, northing, and elevation) in the SfM point cloud.

Next, we repeat the ICP and cloud to cloud differencing tests with this GCP-optimized SfM point cloud and the airborne LiDAR. The incorporated GCPs eliminate much of the apparent warping: 50% of the LiDAR points now deviate vertically from the closest SfM point by <3 cm and 90% by <13 cm (Fig. 10), down from <10 cm and <41 cm without use of GCPs (Fig. 8). Importantly, these new vertical residuals are close to the 5–10 cm spot height uncertainties reported for the B4 LiDAR survey (Toth et al., 2007). While small residuals are still present in areas of high slope, vegetation and around the SfM survey border, the switched stream channels now stand out, indicating genuine morphological change. Even before applying ICP, the tilt of the SfM data set is now corrected. ICP alignment of the GCP-optimized and airborne LiDAR point clouds yields reduced rotational components of <0.003 radians, indicating only marginal tilting. This is demonstrated visually by comparing cross-scarp profiles through each data set with no ICP applied (Fig. 9B). The SfM profile now mimics the slope of the LiDAR profile, the only remaining difference being a slight translational offset of ~0.1 m vertically and ~0.9 m horizontally. Presumably this reflects small registration differences between the local GPS base stations used for each survey.

Tectonic Interpretation of the SfM Topography

We use the detailed SfM topography to evaluate geomorphic offsets on the alluvial fan, also incorporating field observations of fault gouge and fault orientations. Faulting on the fan surface occurs over an ~20-m-wide zone that includes a distinct, southwest-facing scarp (Fig. 11). At the largest scale, the margins of the fan (marked in Fig. 11 by orange lines) are offset right laterally by 20–25 m, providing an estimate for the total slip across the fault zone since deposition of the fan. The total apparent vertical displacement across the scarp, measured from Figure 9B, is ~0.8 m. In the long term, this dip slip has contributed to uplift of the Indio Hills, but it is nevertheless a small component (<5%) of the total slip on the strike-slip fault at this locality. At the smallest scale, a set of incised channels and an intervening bar are offset 2.4–3.3 m right laterally across the southwestern-most scarp only. These channels, very distinct in the SfM but difficult to discern on the B4 LiDAR due to the coarser resolution and corduroy pattern (Fig. 6D), are more incised on the scarp face and downslope fan. This suggests that they were refreshed after older earthquakes produced vertical displacement across the fan surface, and were then offset by the last earthquakes along only the southernmost fault. The magnitude of right-lateral displacement (~3 m) is similar to the average slip estimated for the last event along this section of the San Andreas fault by Madden et al. (2013), and may be the product of the ca. C.E. 1690 earthquake. More generally, these results show that improved topographic data from SfM can be used to augment data sets of small offsets on active faults.

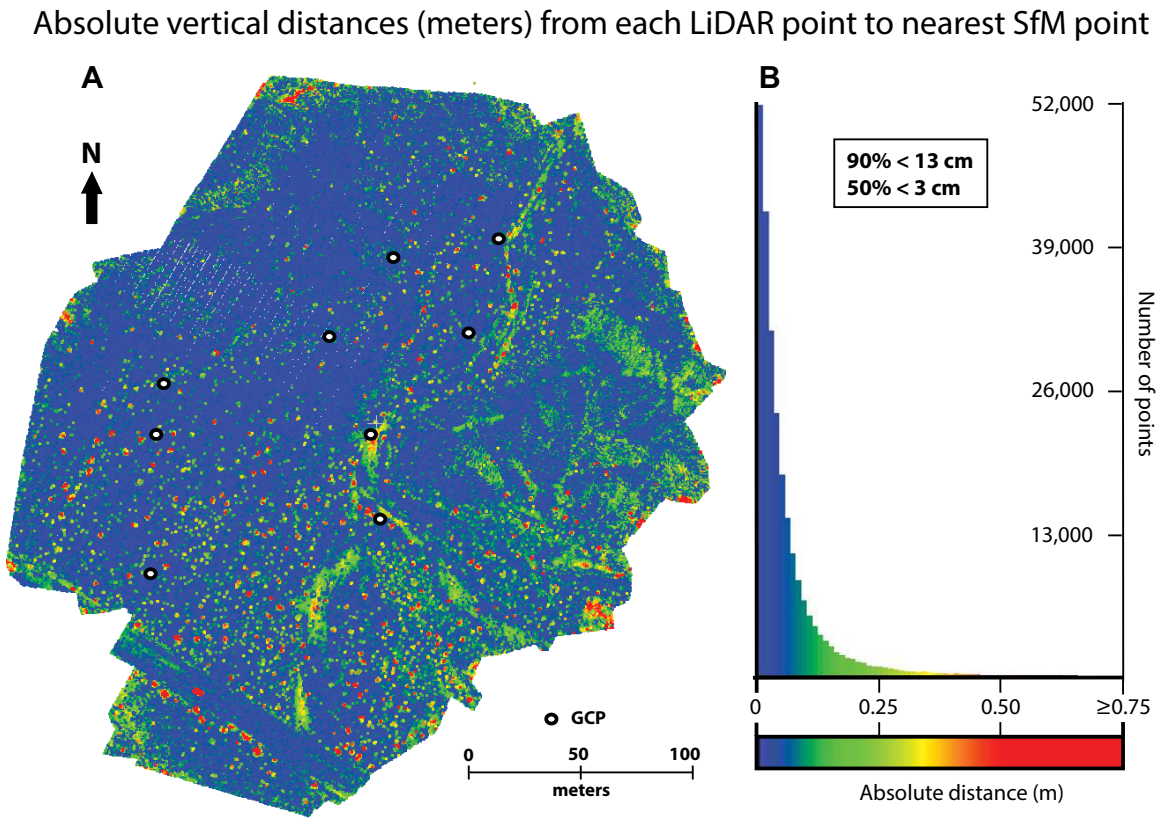

Figure 10. Same plot as in Figure 8, but now using the Washington Street (San Andreas fault) structure from motion (SfM) data set that was optimized with ground control points (GCPs). (A) Map. (B) Histogram. The color scale is the same in both A and B, as well as in Figure 8. White dots indicate locations of the GCPs that were used. Using GCPs reduces most vertical distances to <3 cm, and the worst locations occur at the perimeter of the scene, further from the GCPs and where topography was more rugged. The comparison also highlights some morphological changes in the scene: the red and yellow areas in the main channel probably represent the switching of the active channel (erosion and deposition) between 2005 and 2013 (see Figs. 5C, 5D).

Results: The Galway Lake Road Site on the 1992 Landers Earthquake Rupture

The Galway Lake Road site, centered at 34°32′14″N, 116°33′05″W, covers a short segment of the Emerson fault, which ruptured as part of the 1992 M_w 7.3 Landers earthquake (Fig. 4). The site is close to both the earthquake epicenter and the peak of the measured slip distribution (Sieh et al., 1993), and was chosen to explore the potential for deploying SfM in the immediate aftermath of an earthquake. At this site, the 1992 rupture is marked by a prominent southwest-facing scarp in folded lake bed and alluvial deposits, thought to reflect a reverse faulting component to the coseismic slip. The scarp accommodated a maximum vertical displacement of ~2 m as well as horizontal (dextral) slip of as much as ~4 m and has been monitored for geomorphic change since 1992 (Arrowsmith and Rhodes, 1994).

We surveyed an ~1 km-long section of the surface rupture using the same aerial platforms and camera set-up as at the Washington Street site. Both the helium balloon and motorized kite photosets required about 30 min to set up and 1 h to survey. Here we focus on the 450 photograph balloon data set, which was captured from ~60 m AGL in a traverse along the fault (Fig. 12B). In Photoscan, we used this photoset to produce a point cloud, 90% of which contains >65 points/m^2 and 50% of which contains >530 points/m^2 (at the low-quality setting), as well as a 2-cm-resolution DEM (Fig. 12A). Like the Washington Street site, point density for the Galway Lake Road site increases in areas of higher photo density, and also increases by a factor of two with each increasing level of quality (Fig. 12B).

We compare the SfM topography to an existing, high-density (230 points/m^2) terrestrial LiDAR data set (Fig. 12C) collected in 2008 (for details see Haddad et al., 2012). This GPS-controlled LiDAR survey took trained personnel two days to complete using two scanner units, but covered an area less than half the size of that surveyed by SfM (Fig. 12A). Scanner positions were mostly southwest of the fault and faced northeast, in order to densely sample the scarp face. As a result there are data gaps (shadow zones) on the northeast side of thick bushes, in narrow gullies incised into the scarp footwall, and in a few other regions that were hidden from the scanner line of site. These areas were all densely sampled by SfM (Fig. 12A), although in contrast the LiDAR better characterized the scarp face.

Using the procedure described herein (see discussion of Washington Street site results), we performed an ICP alignment of the overlapping portions of the SfM and terrestrial LiDAR point clouds, and then compared each terrestrial LiDAR point to the nearest SfM point. When only the camera GPS positions were used as geospatial constraints, 90% of vertical

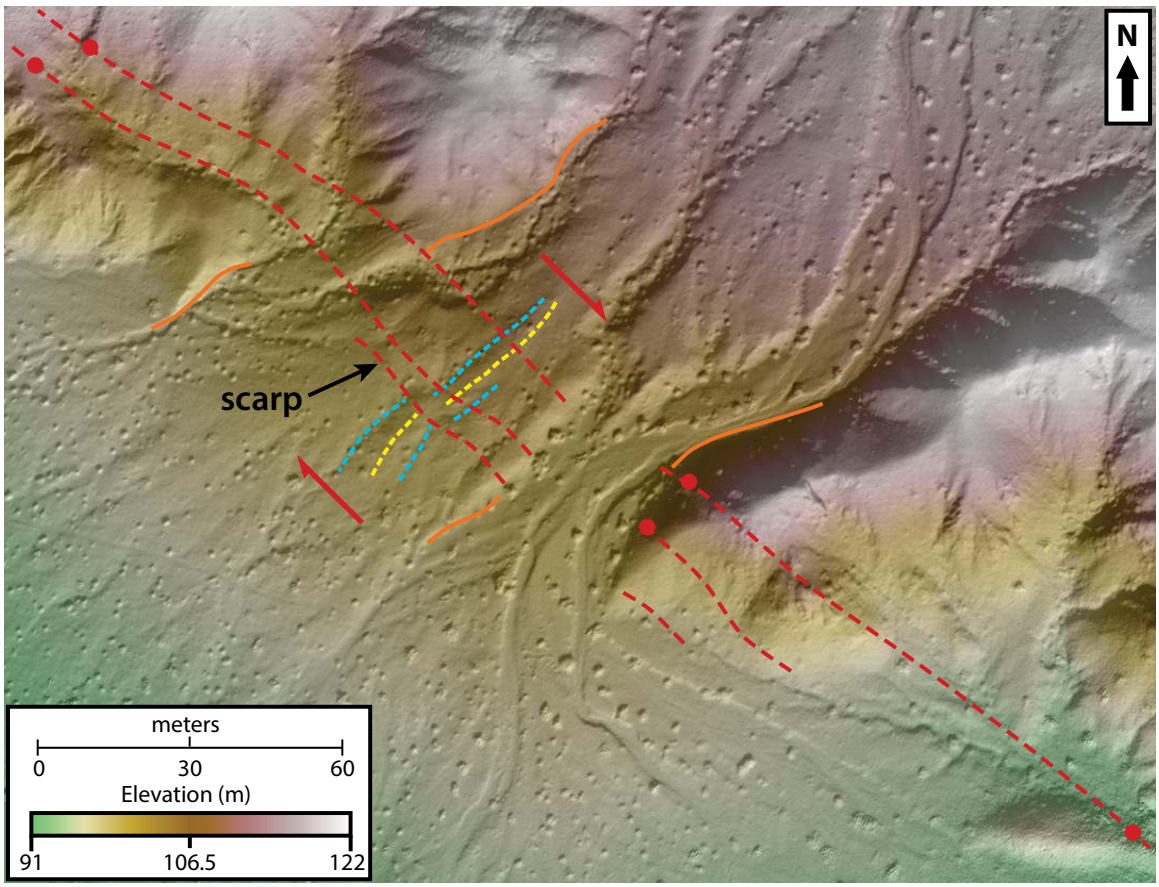

Figure 11. Interpreted structure from motion (SfM) digital elevation model (DEM) of the Washington Street site (San Andreas fault). Red lines mark fault traces that were mapped using a combination of deflected channels and topography evident in the SfM DEM, and field observations of gouge zones (see red dots) and lineaments. The southwestern strand forms a clear scarp with an apparent vertical displacement of ~0.8 m (up on the northeast) and also right-laterally offsets a channel (yellow) and bar (blue) by ~3 m. This is the same scarp profiled in Figure 9. Margins of the fan are outlined in orange and are offset right-laterally by 20–25 m, depending on the projection across the fault zone.

closest point distances are <39 cm and 50% are <8 cm (Figs. 13A, 13C). The largest discrepancies coincide with the northwestern end of the SfM survey, which was reconstructed from a small range of photograph viewpoints. As at the Washington Street site, bushes, steep slopes, and parked vehicles are also marked by higher cloud to cloud distances.

Next, we attempt to reduce these discrepancies by optimizing the overlapping portion of the SfM topography with GCPs. We used nine GCPs sourced directly from the terrestrial LiDAR DEM, each one corresponding to a prominent feature easily identifiable in both data sets. After optimizing the SfM point cloud, the closest point distances are slightly reduced to <32 cm for 90% of the terrestrial LiDAR points and <6 cm for 50% (Figs. 13B, 13C). This indicates that the two data sets are not as closely vertically aligned as the equivalent Washington Street site data sets. We attribute this greater misalignment to the sublinear nature of the Galway Lake Road photoset, which limits the azimuthal coverage of matched features on the ground compared to the lawnmower pattern of photograph collection deployed at the Washington Street site.

DISCUSSION

Having established and tested our workflow for generating high-resolution topography with SfM, we now discuss the outlook for this technology in mapping sparsely vegetated landscapes, with a focus on applications in active tectonics. One powerful application of SfM will be to reveal and characterize subtle geomorphic features that provide information about the fault slip distribution during past earthquakes. Zielke et al. (2010, 2012) and Salisbury et al. (2012) have demonstrated this concept using B4 airborne LiDAR data in central and southern California. SfM is an excellent alternative to LiDAR for such studies, producing denser topographic data than airborne LiDAR and more homogenous spatial coverage than terrestrial LiDAR, with considerably less time spent in the field and less power required to collect the primary data. SfM thus has the potential to provide an unparalleled density of offset measurements at very high accuracy, allowing for improved knowledge of past earthquake slip distributions and thus a better gauge of paleo-earthquake magnitude. These values of slip and magnitude are important to regional seismic hazard analyses (e.g., Arrowsmith et al., 2011; Madden et al., 2013). As it can be deployed quickly, it will also be valuable for post-earthquake documentation of fragile features in fault zones (Gold et al., 2013) and distributed deformation across surface rupture zones (Oskin et al., 2012).

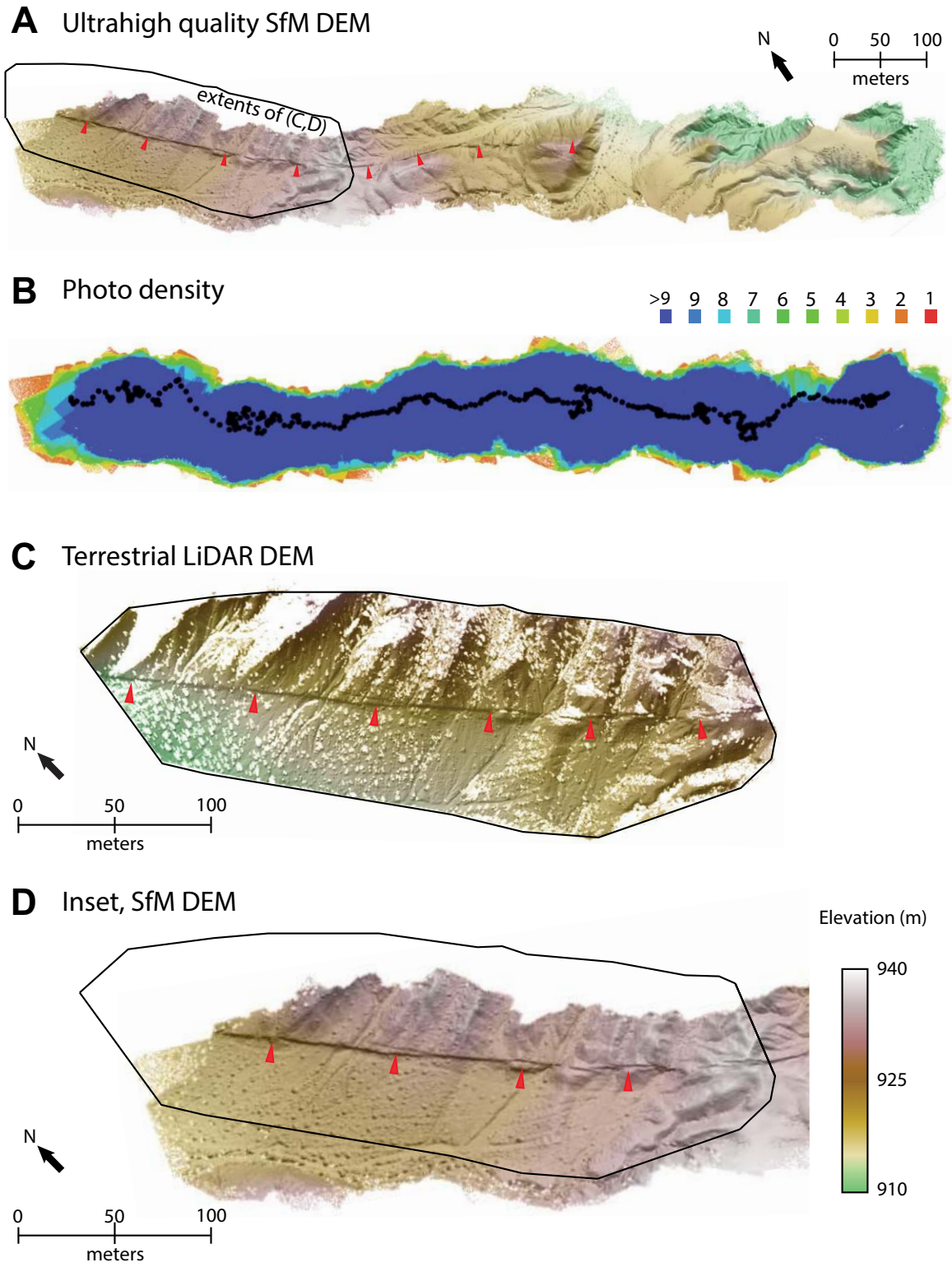

Figure 12. Galway Lake Road site (along the Emerson fault). (A) Structure from motion (SfM) digital elevation model (DEM) built in Photoscan at the ultrahigh-quality setting, artificially illuminated from azimuth 57°, elevation 64°. Red triangles point to the fault scarp generated in the 1992 Landers earthquake. (B) Photograph footprint density plot for the SfM data set. (C) Terrestrial LiDAR (light detection and ranging) DEM of area enclosed by the black polygon in A, gridded at 5 cm resolution in GEON points2grid (Kim et al., 2006) and enlarged to show detail. Details of this data set were provided in Haddad et al. (2012). The elevation scale at bottom right scales both A and C. (D) SfM DEM (area shown in A).

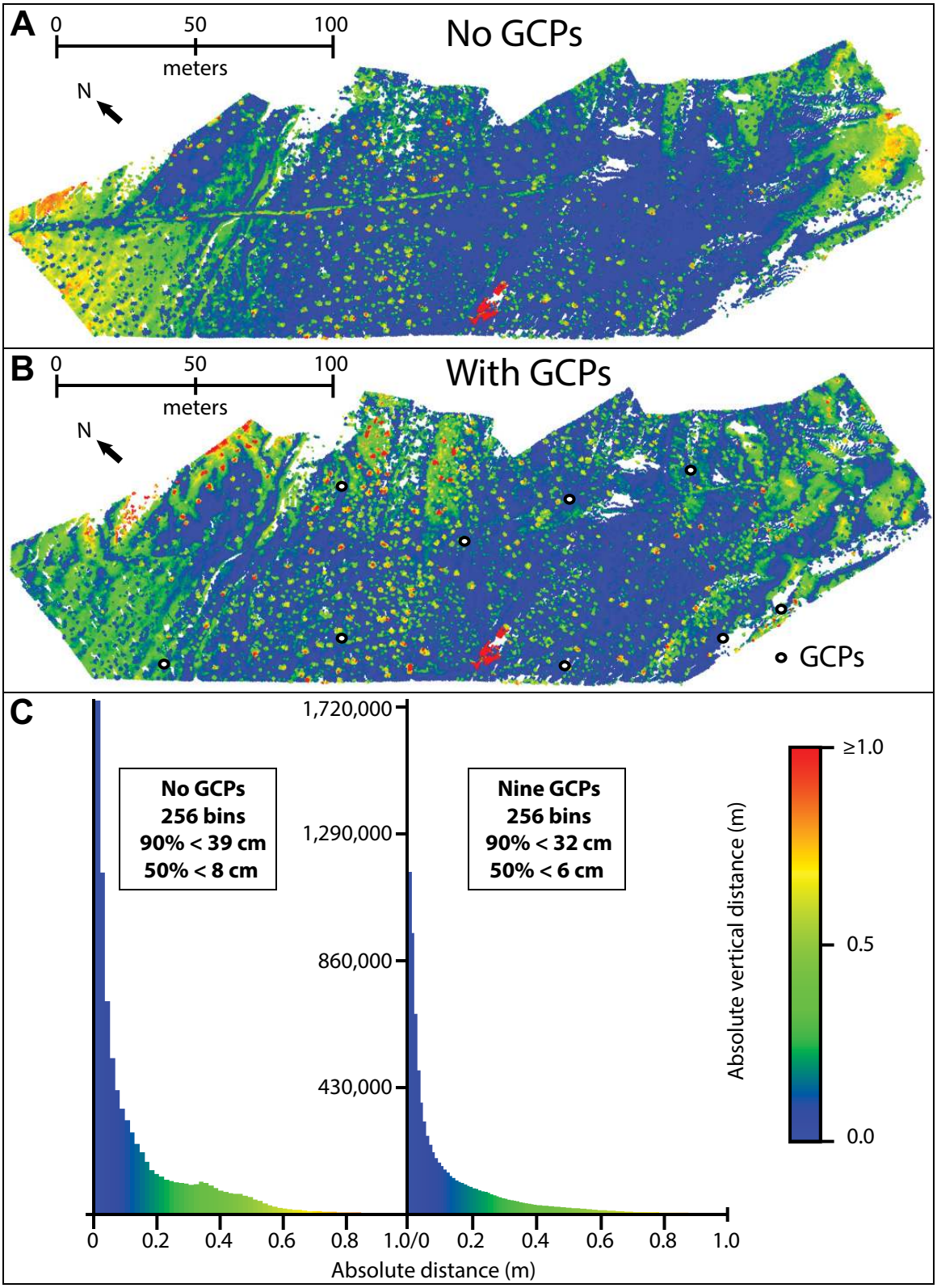

Figure 13. Plots of the vertical distances between each LiDAR (light detection and ranging) point and its closest low-quality structure from motion (SfM) point cloud neighbor at the Galway Lake Road site (along the Emerson fault), and histograms showing the spread in these values across the entire scene. (A) We use the SfM data set that was constructed without ground control points (GCPs). (B) We use the SfM data that were optimized with GCPs (see white circles). (C) Histograms of data from A and B.

A similar application worth investigating with SfM data is scarp degradation modeling, in which the age of, or vertical displacement rate across, an earthquake scarp is estimated through detailed knowledge of its shape and the local rate of sediment diffusion (e.g., Nash, 1980; Hanks et al., 1984). Morphological scarp dating requires high-resolution cross-fault topographic profiles that can be easily extracted from carefully registered SfM topography, including areas where airborne or terrestrial LiDAR surveying is impractical or too expensive. This application is an exemplary case in which SfM will require precisely surveyed GCPs; any warping or tilting to the cross-fault topography profiles (as we observed in Fig. 9) could significantly affect the recovered scarp ages and displacement rates.

The affordability and flexibility of SfM opens up the possibility of using high-resolution topography as a monitoring tool in areas of limited vegetation, in a way that would be difficult, time consuming, and expensive with airborne or terrestrial LiDAR. This capability was demonstrated by James and Robson (2012) in their multitemporal ground-based SfM study of cliff erosion. Aerial SfM systems such as the one we outline here, combined with simple algorithms for differencing topographic data sets (e.g., Leprince et al., 2011; Aryal et al., 2012; Borsa and Minster 2012; Nissen et al., 2012; Lague et al., 2013), could be a powerful new tool for measuring and monitoring detailed 3D fault zone deformation and other related topographic changes such as landsliding, fault scarp degradation, and knickpoint retreat.

CONCLUSIONS

Structure from motion is an affordable and expedient way of generating high-resolution topography in areas of sparse or low-lying vegetation. We use an affordable, aerial platform-based SfM system to map two ~0.1 km^2 sites on southern California faults. Using data collected within just a few hours, we are able to construct textured (colored) point clouds and DEMs with densities of hundreds of points per square meter and resolutions of a few centimeters, respectively. Incorporating a few differential GPS GCPs results in closest point deviations of just a few centimeters between the SfM point clouds and existing airborne and terrestrial LiDAR data, distances that are within the bounds of formal errors in the airborne LiDAR point positions. SfM has rich potential for enabling scientists to map and monitor faulted landscapes in unparalleled detail.

ACKNOWLEDGMENTS

This project was funded by the Southern California Earthquake Center through grants 10526 and 13084. Our highest quality structure from motion (SfM) datasets at both sites are freely available for download (as point clouds or digital elevation models) from the OpenTopography portal (www.opentopography.org), which is supported by the National Science Foundation (NSF) under awards 0930731 and 0930643. All LiDAR (light detection and ranging) data used in the paper were also downloaded from OpenTopography. The B4 LiDAR Project collected point cloud data over the southern San Andreas and San Jacinto faults in southern California. Lidar data acquisition and processing were performed by the National Center for Airborne Laser Mapping in partnership with the U.S. Geological Survey (USGS; led by Ken Hudnut) and Ohio State University (led by Michael Bevis) with funding from the Earth Sciences (EAR) Geophysics program at the NSF. Optech International contributed the ALTM3100 laser scanner system, UNAVCO and SCIGN (Southern California Integrated GPS Network) assisted in global positioning system (GPS) ground control and continuous high-rate GPS data acquisition, and a group of volunteers from the USGS, University of California–San Diego, University of California–Los Angeles, California Institute of Technology, and private industry, as well as gracious landowners along the fault zones, also made the project possible. Terrestrial LiDAR data for the Galway Lake Road scarp were collected by a joint team from the University of Texas–Dallas and Arizona State University with support from NSF grant EAR-0651098. This scan, and our new SfM dataset, build on more than two decades of work at this site led by Dallas Rhodes and Ramon Arrowsmith. Dimitri Lague brought the open source CloudCompare (http://www.danielgm.net/cc/) to our attention, and students at the Understanding Earth-Surface Processes in the Alpine Environment from High-Resolution Topography European Geosciences Union summer school (http://intra.tesaf.unipd.it/cms/summeregu2013/) showed Arrowsmith how well it could work for these purposes. We thank Brance Hudzietz and Yucong Lin for their help in the field; several other colleagues, including Chris Crosby, Emily Kleber, Mike Oskin, and Barrett Salisbury, for many fruitful discussions; and Ryan Gold and Scott Bennett for careful initial reviews of the manuscript. We also thank an anonymous reviewer, Nico Hardebol, and Shanaka de Silva for their reviews for *Geosphere*. Any use of trade, firm, or product names is for descriptive purposes only and does not imply endorsement by the U.S. Government.

REFERENCES CITED

Arrowsmith, J.R., and Rhodes, D.D., 1994, Original forms and initial modifications of the Galway Lake Road scarp formed along the Emerson fault during the 28 June 1992 Landers, California, earthquake: Seismological Society of America Bulletin, v. 84, no. 3, p. 511–527.

Arrowsmith, R., Madden, C., Haddad, D.E., Salisbury, J.B., and Weldon, R.J., 2011, Compilation of slip in last earthquake data for high-slip rate faults in California for input into slip dependent rupture forecast: American Geophysical Union, Fall Meeting, abs. S13B-06.

Aryal, A., Brooks, B.A., Reid, M.E., Bawden, G.W., and Pawlak, G.R., 2012, Displacement fields from point cloud data: Application of particle imaging velocimetry to landslide geodesy: Journal of Geophysical Research, v. 117, no. F1, F01029, doi:10.1029/2011JF002161.

Barth, N.C., Toy, V.G., Langridge, R.M., and Norris, R.J., 2012, Scale dependence of oblique plate-boundary partitioning: New insights from LiDAR, central Alpine fault, New Zealand: Lithosphere, v. 4, p. 435–448, doi:10.1130/L201.1.

Besl, P.J., and McKay, N.D., 1992, Method for registration of 3-D shapes: IEEE Transactions on Pattern Analysis and Machine Intelligence, v. 14, p. 239–256, doi:10.1109/34.121791.

Bevis, M., and 19 others, 2005, The B4 Project: Scanning the San Andreas and San Jacinto fault zones: Eos (Transactions, American Geophysical Union) v. 86, Fall meeting supplement, abs. H34B–01.

Bielecki, A.E., and Mueller, K.J., 2002, Origin of terraced hillslopes on active folds in the southern San Joaquin Valley, California: Geomorphology, v. 42, p. 131–152, doi:10.1016/S0169-555X(01)00082-4.

Borsa, A., and Minster, J.B., 2012, Rapid determination of near-fault earthquake deformation using differential Lidar: Seismological Society of America Bulletin, v. 102, p. 1335–1347, doi:10.1785/0120110159.

Brooks, B.A., Glennie, C., Hudnut, K.W., Ericksen, T., and Hauser, D., 2013, Mobile laser scanning applied to the earth sciences: Eos (Transactions, American Geophysical Union), v. 94, no. 36, p. 313–315, doi:10.1002/2013EO360002.

Chen, Y., and Medioni, G., 1992, Object modelling by registration of multiple range images: Image and Vision Computing, v. 10, no. 3, p. 145–155, doi:10.1016/0262-8856(92)90066-C.

Cook, K., 2013, Quantifying fluvial bedrock erosion using repeat terrestrial Lidar: European Geosciences Union General Assembly Conference abstract EGU2013–2744.

Cunningham, D., Grebby, S., Tansey, K., Gosar, A., and Kastelic, V., 2006, Application of airborne LiDAR to mapping seismogenic faults in forested mountainous terrain, southeastern Alps, Slovenia: Geophysical Research Letters, v. 33, no. 20, L20308, doi:10.1029/2006GL027014.

DeLong, S.B., Prentice, C.S., Hilley, G.E., and Ebert, Y., 2012, Multitemporal ALSM change detection, sediment delivery, and process mapping at an active earthflow: Earth Surface Processes and Landforms, v. 37, p. 262–272, doi:10.1002/esp.2234.

d'Oleire-Oltmanns, S., Marzol, I., Peter, K., and Ries, J., 2012, Unmanned Aerial Vehicle (UAV) for monitoring soil erosion in Morocco: Remote Sensing, v. 4, p. 3390–3416, doi:10.3390/rs4113390.

Duffy, B., Quigley, M., Barrell, D.J., Van Dissen, R., Stahl, T., Leprince, S., McInnes, C., and Bilderback, E., 2013, Fault kinematics and surface deformation across a releasing bend during the 2010 M_W 7.1 Darfield, New Zealand, earthquake revealed by differential LiDAR and cadastral surveying: Geological Society of America Bulletin, v. 125, p. 420–431, doi:10.1130/B30753.1.

Elliott, A.J., Gold, P.O., Styron, R.H., Oskin, M.E., Taylor, M.H., Hinojosa-Corona, A., and Herrs, A.J., 2011, Time-series of scarp modification on the 2010 El Mayor–Cucapah earthquake rupture from repeat terrestrial LiDAR surveys: American Geophysical Union Fall meeting, abs. T31B–2352.

Elliott, J.R., Nissen, E.K., England, P.C., Jackson, J.A., Lamb, S., Li, Z., Oehlers, M., and Parsons, B., 2012, Slip in the 2010–2011 Canterbury earthquakes, New Zealand: Journal of Geophysical Research, v. 117, B03401, doi:10.1029/2011JB008868.

Ewing, R.C., Smith, V.B., Mohrig, D.C., and Kocurek, G., 2010, Utilization of time series airborne LiDAR to quantify patterns of deposition and erosion across dune-dune interactions at White Sands Dune Field, New Mexico: American Geophysical Union Fall meeting, abs. NG43F–1445.

Fonstad, M.A., Dietrich, J.T., Courville, B.C., Jensen, J.L., and Carbonneau, P.E., 2013, Topographic structure from motion: A new development in photogrammetric measurement: Earth Surface Processes and Landforms, v. 38, p. 421–430, doi:10.1002/esp.3366.

Frankel, K.L., and Dolan, J.F., 2007, Characterizing arid region alluvial fan surface roughness with airborne laser swath mapping digital topographic data: Journal of Geophysical Research, v. 112, no. F2, p. F02025, doi:10.1029/2006JF000644.

Fumal, T.E., Weldon, R.J., Biasi, G.P., Dawson, T.E., Seitz, G.G., Frost, W.T., and Schwartz, D.P., 2002, Evidence for large earthquakes on the San Andreas fault at the Wrightwood, California, paleoseismic site: AD 500 to present: Seismological Society of America Bulletin, v. 92, p. 2726–2760, doi:10.1785/0120000608.

Gold, P.O., Oskin, M.E., Elliott, A.J., Hinojosa-Corona, A., Taylor, M.H., Kreylos, O., and Cowgill, E., 2013, Coseismic slip variation assessed from terrestrial LiDAR scans of the El Mayor–Cucapah surface rupture: Earth and Planetary Science Letters, v. 366, p. 151–162, doi:10.1016/j.epsl.2013.01.040.

Gold, R.D., Cowgill, E., Arrowsmith, J.R., Chen, X., Sharp, W., Cooper, K., and Wang, X., 2011, Faulted terrace risers place new constraints on the late Quaternary slip rate for the central Altyn Tagh fault, northwest Tibet: Geological Society of America Bulletin, v. 123, p. 958–978, doi:10.1130/B30207.1.

Haddad, D.E., Akciz, S.O., Arrowsmith, J.R., Rhodes, D.D., Oldow, J.S., Zielke, O., Toke, N.A., Haddad, A.G., Mauer, J., and Shilpakar, P., 2012, Applications of airborne and terrestrial laser scanning to paleoseismology: Geosphere, v. 8, p. 771–786, doi:10.1130/GES00701.1.

Haller, K.M., Machette, M.N., Dart, R.L., and Rhea, B.S., 2004, US Quaternary fault and fold database released: Eos (Transactions, American Geophysical Union), v. 85, no. 22, p. 218.

Hanks, T.C., Bucknam, R.C., Lajoie, K.R., and Wallace, R.E., 1984, Modification of wave-cut and faulting-controlled landforms: Journal of Geophysical Research, v. 89, p. 5771–5790, doi:10.1029/JB089iB07p05771.

Harwin, S., and Lucieer, A., 2012, Assessing the accuracy of georeferenced point clouds produced via multi-view stereopsis from unmanned aerial vehicle imagery: Remote Sensing, v. 4, p. 1573–1599, doi:10.3390/rs4061573.

Haugerud, R.A., Harding, D.J., Johnson, S.Y., Harless, J.L., Weaver, C.S., and Sherrod, B.L., 2003, High-resolution LiDAR topography of the Puget Lowland, Washington: GSA Today, v. 13, no. 6, p. 4–10, doi:10.1130/1052-5173(2003)13<0004:HLTOTP>2.0.CO;2.

Hayakawa, Y.S., Oguchi, T., and Lin, Z., 2008, Comparison of new and existing global digital elevation models: ASTER G-DEM and SRTM-3: Geophysical Research Letters, v. 35, L17404, doi:10.1029/2008GL035036.

Hilley, G.E., and Arrowsmith, J.R., 2008, Geomorphic response to uplift along the Dragon's Back pressure ridge, Carrizo Plain, California: Geology, v. 36, p. 367–370, doi:10.1130/G24517A.1.

Hilley, G.E., DeLong, S., Prentice, C., Blisniuk, K., and Arrowsmith, J.R., 2010, Morphologic dating of fault scarps using airborne laser swath mapping (ALSM) data: Geophysical Research Letters, v. 37, no. 4, L04301, doi:10.1029/2009GL042044.

Howle, J.F., Bawden, G.W., Schweickert, R.A., Finkel, R.C., Hunter, L.E., Rose, R.S., and von Twistern, B., 2012, Airborne LiDAR analysis and geochronology of faulted glacial moraines in the Tahoe-Sierra frontal fault zone reveal substantial seismic hazards in the Lake Tahoe region, California-Nevada, USA: Geological Society of America Bulletin, v. 124, p. 1087–1101, doi:10.1130/B30598.1.

Hudnut, K.W., Borsa, A., Glennie, C., and Minster, J.B., 2002, High-resolution topography along surface rupture of the 16 October 1999 Hector mine, California, earthquake (Mw 7.1) from airborne laser swath mapping: Seismological Society of America Bulletin, v. 92, p. 1570–1576, doi:10.1785/0120000934.

Hugenholtz, C.H., Moorman, B.J., Riddell, K., and Whitehead, K., 2012, Small unmanned aircraft systems (sUAS) for remote sensing: Eos (Transactions, American Geophysical Union), v. 93, no. 25, p. 236–237, doi:10.1029/2012EO250005.

Hurst, M.D., Mudd, S.M., Attal, M., and Hilley, G., 2013, Hillslopes record the growth and decay of landscapes: Science, v. 341, p. 868–871, doi:10.1126/science.1241791.

Jaboyedoff, M., Oppikofer, T., Abellán, A., Derron, M.H., Loye, A., Metzger, R., and Pedrazzini, A., 2012, Use of LIDAR in landslide investigations: A review: Natural Hazards, v. 61, p. 5–28, doi:10.1007/s11069-010-9634-2.

James, M.R., and Robson, S., 2012, Straightforward reconstruction of 3D surfaces and topography with a camera: Accuracy and geoscience application: Journal of Geophysical Research, v. 117, F03017, doi:10.1029/2011JF002289.

Karabacak, V., Altunel, E., and Cakir, Z., 2011, Monitoring aseismic surface creep along the North Anatolian fault (Turkey) using ground-based LIDAR: Earth and Planetary Science Letters, v. 304, p. 64–70, doi:10.1016/j.epsl.2011.01.017.

Kim, H., Arrowsmith, J.R., Crosby, C.J., Jaeger-Frank, E., Nandigam, V., Memon, A., Conner, J., Badden, S.B., and Baru, C., 2006, An efficient implementation of a local binning algorithm for digital elevation model generation of LiDAR/ALSM data: American Geophysical Union Fall meeting, abs. G53C–0921.

Kogan, L., and Bendick, R., 2011, A mass failure model for the initial degradation of fault scarps, with application to the 1959 scarps at Hebgen Lake, Montana: Seismological Society of America Bulletin, v. 101, p. 68–78, doi:10.1785/0120100107.

Kondo, H., Toda, S., Okumura, K., Takada, K., and Chiba, T., 2008, A fault scarp in an urban area identified by LiDAR survey: A case study on the Itoigawa–Shizuoka Tectonic Line, central Japan: Geomorphology, v. 101, p. 731–739, doi:10.1016/j.geomorph.2008.02.012.

Lague, D., Brodu, N., and Leroux, J., 2013, Accurate 3D comparison of complex topography with terrestrial laser scanner: Application to the Rangitikei canyon (NZ): ISPRS Journal of Photogrammetry and Remote Sensing, v. 82, p. 10–26, doi:10.1016/j.isprsjprs.2013.04.009.

Leprince, S., Hudnut, K.W., Akciz, S.O., Hinojosa-Corona, A., and Fletcher, J.M., 2011, Surface rupture and slip variation induced by the 2010 El Mayor–Cucapah earthquake, Baja California, quantified using COSI-Corr analysis on pre-and post-earthquake LiDAR acquisitions: American Geophysical Union Fall meeting, abs. EP41A–0596.

Lin, Z., Kaneda, H., Mukoyama, S., Asada, N., and Chiba, T., 2013, Detection of subtle tectonic geomorphic features in densely forested mountains by very high-resolution airborne LiDAR survey: Geomorphology, v. 182, p. 104–115, doi:10.1016/j.geomorph.2012.11.001.

Lowe, D., 2004, Distinctive image features from scale-invariant keypoints: International Journal of Computer Vision, v. 60, p. 91–110, doi:10.1023/B:VISI.0000029664.99615.94.

Madden, C., Haddad, D.E., Salisbury, J.B., Zielke, O., Arrowsmith, J.R., Weldon, R.J., and Colunga, J., 2013, Appendix R—Compilation of slip-in-the-last-event data and analysis of last event, repeated slip, and average displacement for recent and prehistoric ruptures: U.S. Geological Survey Open-File Report 2013–1165, 65 p.

McGarey, P., and Saripalli, S., 2013, AUTOKITE: Experimental use of a low cost autonomous kite plane for aerial photography and reconnaissance: Journal of Intelligent and Robotic Systems, v. 74, p. 363–370.

Meigs, A., 2013, Active tectonics and the LiDAR revolution: Lithosphere, v. 5, p. 226–229, doi:10.1130/RF.L004.1.

Nash, D.B., 1980, Morphologic dating of degraded normal fault scarps: Journal of Geology, v. 88, p. 353–360, doi:10.1086/628513.

Niethammer, U., James, M.R., Rothmund, S., Travelletti, J., and Joswig, M., 2012, UAV-based remote sensing of the Super-Sauze landslide: Evaluation and results: Engineering Geology, v. 128, p. 2–11, doi:10.1016/j.enggeo.2011.03.012.

Nissen, E., Krishnan, A.K., Arrowsmith, J.R., and Saripalli, S., 2012, Three-dimensional surface displacements and rotations from differencing pre- and post-earthquake LiDAR point clouds: Geophysical Research Letters, v. 39, L16301, doi:10.1029/2012GL052460.

Oskin, M.E., Arrowsmith, J.R., Corona, A.H., Elliott, A.J., Fletcher, J.M., Fielding, E.J., Gold, P.O., Garcia, J.J.G., Hudnut, K.W., and Liu-Zeng, J., 2012, Near-field deformation from the El Mayor–Cucapah earthquake revealed by differential LIDAR: Science, v. 335, p. 702–705, doi:10.1126/science.1213778.

Prentice, C.S., Mann, P., Crone, A.J., Gold, R.D., Hudnut, K.W., Briggs, R.W., Koehler, R.D., and Jean, P., 2010, Seismic hazard of the Enriquillo–Plantain Garden fault in Haiti inferred from palaeoseismology: Nature Geoscience, v. 3, p. 789–793, doi:10.1038/ngeo991.

Quigley, M., Van Dissen, R., Litchfield, N., Villamor, P., Duffy, B., Barrell, D., Furlong, K., Stahl, T., Bilderback, E., and Noble, D., 2012, Surface rupture during the 2010 Mw 7.1 Darfield (Canterbury) earthquake: Implications for fault rupture dynamics and seismic-hazard analysis: Geology, v. 40, p. 55–58, doi:10.1130/G32528.1.

Ridgway, J.R., Minster, J.B., Williams, N., Bufton, J.L., and Krabill, W.B., 1997, Airborne laser altimeter survey of Long Valley, California: Geophysical Journal International, v. 131, p. 267–280, doi:10.1111/j.1365-246X.1997.tb01221.x.

Rosnell, T., and Honkavaara, E., 2012, Point cloud generation from aerial image data acquired by a quadrocopter type micro unmanned aerial vehicle and a digital still camera: Sensors, v. 12, p. 453–480, doi:10.3390/s120100453.

Salisbury, J.B., Rockwell, T.K., Middleton, T.J., and Hudnut, K.W., 2012, LiDAR and field observations of slip distribution for the most recent surface ruptures along the central San Jacinto fault: Seismological Society of America Bulletin, v. 102, p. 598–619, doi:10.1785/0120110068.

Scharer, K.M., Salisbury, J.B., Arrowsmith, J.R., and Rockwell, T.K., 2014, Southern San Andreas fault evaluation field activity: Approaches to measuring small geomorphic offsets—challenges and recommendations for active fault studies: Seismological Research Letters, v. 85, p. 68–76.

Scheidl, C., Rickenmann, D., and Chiari, M., 2008, The use of airborne LiDAR data for the analysis of debris flow events in Switzerland: Natural Hazards and Earth System Sciences, v. 8, p. 1113–1127, doi:10.5194/nhess-8-1113-2008.

Shrestha, R.L., Carter, W.E., Lee, M., Finer, P., and Sartori, M., 1999, Airborne laser swath mapping: Accuracy assessment for surveying and mapping applications: Surveying and Land Information Systems, v. 59, p. 83–94.

Shrestha, R.L., Carter, W.E., Sartori, M., Luzum, B.J., and Slatton, K.C., 2005, Airborne laser swath mapping: Quantifying changes in sandy beaches over time scales of weeks to years: ISPRS Journal of Photogrammetry and Remote Sensing, v. 59, p. 222–232, doi:10.1016/j.isprsjprs.2005.02.009.

Sieh, K., and 19 others, 1993, Near-field investigations of the Landers earthquake sequence, April to July 1992: Science, v. 260, no. 5105, p. 171–176, doi:10.1126/science.260.5105.171.

Snavely, N., Seitz, S.N., and Szeliski, R., 2008, Modeling the world from internet photo collections: International Journal of Computer Vision, v. 80, p. 189–210, doi:10.1007/s11263-007-0107-3.

Spaete, L.P., Glenn, N.F., Derryberry, D.R., Sankey, T.T., Mitchell, J.J., and Hardegree, S.P., 2011, Vegetation and slope effects on accuracy of a LiDAR-derived DEM in the sagebrush steppe: Remote Sensing Letters, v. 2, p. 317–326, doi:10.1080/01431161.2010.515267.

Thoma, D.P., Gupta, S.C., Bauer, M.E., and Kirchoff, C.E., 2005, Airborne laser scanning for riverbank erosion assessment: Remote Sensing of Environment, v. 95, p. 493–501, doi:10.1016/j.rse.2005.01.012.

Toth, C., Brzezinska, D., Csanyi, N., Paska, E., and Yastikli, N., 2007, LiDAR mapping supporting earthquake research of the San Andreas fault, *in* Proceedings, ASPRS 2007 Annual Conference: Bethesda, Maryland, American Society for Photogrammetry and Remote Sensing, p. 1–11.

Turner, D., Lucieer, A., and Watson, C., 2012, An automated technique for generating georectified mosaics from ultra-high resolution unmanned aerial vehicle (UAV) imagery, based on Structure from Motion (SfM) point clouds: Remote Sensing, v. 4, p. 1392–1410, doi:10.3390/rs4051392.

Verhoeven, G., 2011, Taking computer vision aloft—Archaeological three-dimensional reconstructions from aerial photographs with photoscan: Archaeological Prospection, v. 18, p. 67–73, doi:10.1002/arp.399.

Wang, C., and Glenn, N., 2009, Integrating LiDAR intensity and elevation data for terrain characterization in a forested area: IEEE Geoscience and Remote Sensing Letters, v. 6, p. 463–466, doi:10.1109/LGRS.2009.2016986.

Westoby, M.J., Brasington, J., Glasser, N.F., Hambrey, M.J., and Reynolds, J.M., 2012, 'Structure-from-Motion' photogrammetry: A low-cost, effective tool for geoscience applications: Geomorphology, v. 179, p. 300–314, doi:10.1016/j.geomorph.2012.08.021.

Wilkinson, M., and 11 others, 2010, Partitioned postseismic deformation associated with the 2009 Mw 6.3 L'Aquila earthquake surface rupture measured using a terrestrial laser scanner: Geophysical Research Letters, v. 37, L10309, doi:10.1029/2010GL043099.

Zielke, O., Arrowsmith, J.R., Ludwig, L.G., and Akciz, S.O., 2010, Slip in the 1857 and earlier large earthquakes along the Carrizo Plain, San Andreas fault: Science, v. 327, p. 1119–1122, doi:10.1126/science.1182781.

Zielke, O., Arrowsmith, J.R., Grant-Ludwig, L.B., and Akciz, S.O., 2012, High resolution topography-derived offset along the 1857 Fort Tejon earthquake rupture trace, San Andreas fault: Seismological Society of America Bulletin, v. 102, p. 1135–1154, doi:10.1785/0120110230.